



Available online at www.sciencedirect.com

ScienceDirect

Comput. Methods Appl. Mech. Engrg. 312 (2016) 596–634

**Computer methods
in applied
mechanics and
engineering**

www.elsevier.com/locate/cma

Stochastic analysis of polymer composites rupture at large deformations modeled by a phase field method

Jie Wu^{a,b}, Colin McAuliffe^b, Haim Waisman^{b,*}, George Deodatis^b

^a State Key Laboratory of disaster reduction in Civil Engineering, Department of Geotechnical Engineering, Tongji University, Shanghai, 200092, China

^b Department of Civil Engineering and Engineering Mechanics, Columbia University, 610 Seeley W. Mudd Building, 500 West 120th Street, Mail Code 4709, New York, NY 10027, United States

Available online 22 June 2016

Abstract

Carbon black reinforced natural rubber is a composite material that is increasingly being used in engineering applications. Carbon black is orders of magnitude stiffer than natural rubber, resulting in a composite material with increased stiffness, but decreased fracture strain. Detailed knowledge of the relationship between the composition of reinforced rubber and its fracture toughness is important for analysis and design of various engineering systems. To this end, the Arruda–Boyce model is adopted for modeling the hyperelastic rubber matrix and a Neo-Hookean model is used for the reinforcing particles. A phase field method is then employed to simulate damage nucleation and propagation under quasi-static loading. The phase field method is well suited for such problems, since it can capture complex patterns of damage nucleation, coalescence, and propagation. The phase field hyperelastic model is validated on a set of experimental data available in the literature. To quantify the uncertainty in the failure of these materials, a Monte Carlo simulation is carried out with random ellipsoidal particles distribution. Each realization undergoes large stretching up to failure, where force–displacement curves and fracture surface energies are recorded. Failure of a sample is defined as the point for which the load drops to 75% of its peak value. Numerical examples of stiff inclusions and voids are considered and the composite response is examined on an intact and pre-notched unit cells. The stochastic analysis reveals the statistical distributions corresponding to the rupture of polymer composites and provides insight into better design of these materials.

© 2016 Elsevier B.V. All rights reserved.

Keywords: Phase field method; Crack nucleation; Monte Carlo simulation; Polymer composites; Hyperelasticity; Large deformations

1. Introduction

Composite materials are increasingly being used in current engineering applications due to their attractive properties such as a high strength to weight ratio and low cost. Carbon black (CB) reinforced natural rubber (NR)

* Corresponding author.

E-mail address: waisman@civil.columbia.edu (H. Waisman).

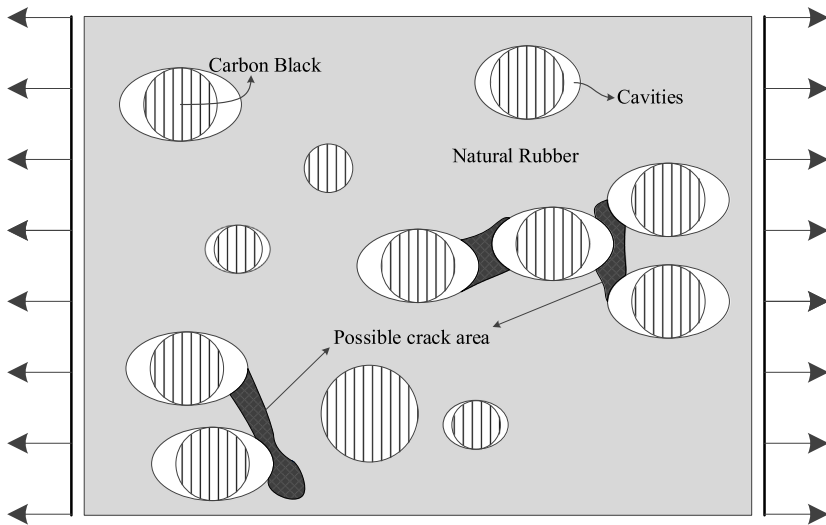


Fig. 1. Schematic illustration of Carbon black (CB) reinforced natural rubber (NR). The applied load causes decohesion of the polymer matrix from some of the particles which result in cavities, formation of cracks and rupture of the composite.

is a composite material, whose macro mechanical properties depend on its micro composition. In order to study the relationship between fracture toughness of CB reinforced NR and its compositions, different physical experiments have been carried out. Sajjayanukul et al. [1] investigated the processability and viscoelastic properties of NR compounds filled with different CB loadings and types. It was found that the type and amount of CB strongly influence the viscoelastic properties of rubber compounds. In the experimental work by Teh et al. [2], scanning electron microscopy (SEM) revealed that incorporation of various types of fillers (including organoclay, silica and CB) has transformed the failure mechanism of the resulting vulcanized NR compared to the vulcanized gum. Le Cam et al. [3] studied fatigue crack growth in a CB filled polyisoprene rubber under relaxing loading conditions. It was established that fatigue damage is mostly due to cavitation induced by the de-cohesion between zinc oxides and the rubber matrix. Similar results were observed in the work by Bazhenov et al. [4]. The ductility of a calcium carbonate-filled amorphous copolyester PETG was examined to study the ductile-to-quasi-brittle transition with the increase of volume fraction of filler material.

A schematic illustration of a crack growth mechanism, introduced in [3,4], is illustrated in Fig. 1. The applied load causes decohesion of the polymer matrix from some of the particles which result in cavities, formation and coalescence of cracks and rupture of the composite.

While experimental work is crucial in understanding the mechanism that governs the rupture of the composite, the amount of samples that can be tested is limited and hence might be insufficient to statistically understand the role of spatial distribution of particles on its overall fracture properties. Over the past decades, analytical and computational multiscale homogenization techniques have emerged. For example, Herve and Zaoui [5] developed an analytical homogenization method and obtained the elastic strain and stress fields for n-layered isotropic spherical inclusion embedded in an infinite medium matrix. The model was subjected to uniform stress or strain conditions at infinity. More recently, Omnes et al. [6] predicted the elastic properties (both Young's and bulk moduli) of a CB reinforced NR with a self-consistent model.

Besides the analytical methods, computational homogenization and multiscale methods have also gained significant attention in recent decades. For example many of the computational methods are based on the mathematical homogenization theory using asymptotic expansion techniques [7–11]. This approach has been successfully employed for the simulation of linear materials [12–14] and non-linear materials [15,16]. Another well known method is the multiscale FE^2 method, developed by Feyel et al. [17,18], which for example was used to model the behavior of structures reinforced by long fiber SiC/Ti composite materials with a periodic microstructure.

Verhoosel et al. [19,20] proposed a multiscale failure analysis approach, in which the macroscopic bulk is assumed to be homogeneous, with effective properties obtained by continuous computational homogenization methods. In this approach, a crack is inserted at the macroscale once the macroscopic stresses meet a failure criterion.

Numerical simulations of composite materials rupture were also carried out by Nguyen et al. [21,22] via a nonlocal continuum damage theory. Furthermore, to reduce the computational cost, a novel model reduction approach combining the asymptotic expansion method with the transformation field analysis was proposed based on Eigendeflection concepts [23–25].

Stochastic homogenization is another multiscale approach used to analyze heterogeneous materials response taking into account the randomness of the microstructure. The mechanical properties of polymer nano composites were calculated by a multiscale Monte Carlo finite element method in the work of Spanos and Kotsos [26]. Jacob et al. [27] proposed a practical nonintrusive multiscale solver that permits consideration of uncertainties in heterogeneous materials without exhausting the available computational resources. Bogdanor et al. [28] investigate the use of Bayesian statistical methods for calibration and uncertainty quantification in rate-dependent damage modeling of composite materials. A multiscale stochastic failure analysis for fiber reinforced composites was presented in [29] and the effect of random spatial distribution of constituents was reported. More recently, a three-dimensional, hierarchically parallel, finite strain multiscale solver capable of computing more than 500 million nonlinear equations was developed by Mosby and Matouš [30].

The extended finite element method (XFEM), another important method for modeling discontinuities, was also applied to heterogeneous polymer materials in a multiscale framework [31]. With the data obtained from digital images of material microstructures, the XFEM coupled with the level sets method, was applied to analyze microstructures to obtain homogenized properties for heterogeneous structures [32].

In the work of Hiriyur et al. [33], the XFEM coupled with a Monte Carlo approach was proposed to quantify the uncertainty in the homogenized effective elastic properties of multiphase materials. Savvas et al. [34] expanded this method to more generalized shapes of inclusions. Also based on XFEM, Pike et al. [35,36] formulated and implemented a failure model for random short microfiber reinforced composite materials, and the interactions between fibers were reported. Radtke et al. [37] presented a partition of unity finite element method for simulating non-linear debonding and matrix failure in thin fiber composites. Another non concurrent multiscale framework for hyperelastic heterogeneous microstructures is the nonlinear stochastic homogenization method by Clément et al. [38,39].

Recently, an important method for fracture mechanics, considered by some as a subset of Continuum Damage Mechanics, the so called Phase Field Method (PFM), was developed and employed for the simulation of quasi-static cracks [40], dynamic cracks [41], shear band modeling [42,43], and the finite deformation of rubber materials [44]. With the phase field method, a crack is approximated as a continuous entity, whose width is defined by a small process zone parameter l_0 . It is thus possible to approximate the fracture energy with a volume integral, which does not require a procedure for tracking the crack surface. It has been shown by Bourdin et al. [45] and Francfort and Marigo [46] that at the limit as the process zone parameter tends to zero, the phase field approximation converges to the fracture energy of a discontinuous crack. Moreover, the nucleation of cavities and crack propagation, as well as crack branching and coalescence could be simulated in a straightforward manner with this method. For these reasons, it is a natural choice for the stochastic failure analysis of CB reinforced NR.

In this paper, a MC simulation is performed on hyperelastic materials with CB inclusions together with the phase field method for fracture. Every sample realization of CB reinforced NR undergoes large stretching until failure. Cavities nucleation leading to crack initiation and propagation are studied. The stretch and fracture energy are sampled and plotted at two points of the deformation history. The first point is at the peak of the force–displacement curve and the second is at the point of failure which in our work is defined when the force drops below 75% of the peak value. The overall distributions of the force, stretch and fracture energy at the peak force and at failure are studied and summarized. This provides insight into the fracture response of CB reinforced NR, so called property–structure relationships.

This paper is organized in the following way: in Section 2, the PFM formulation for hyperelasticity at large strains is described. Strong and weak forms of the phase field method are derived and the corresponding spatial discretization and monolithic solution is presented. Two examples that validate the phase field hyperelastic model are discussed in Section 3 along with the modeling assumptions. In Section 4, a brief introduction to the MC simulation as well as a new algorithm to generate realizations with random microstructures is discussed. Sample realizations with different volume fraction or particle/matrix Young's modulus ratio are studied in Section 5. The results are reported and discussed in Section 5.4, including the implication of the failure analysis results for material design. Finally, closing remarks are provided.

2. The phase field method for hyperelasticity

2.1. The strong form of phase field method at large strains

Balance laws. Under quasistatic loadings, inertia terms are neglected and the macro force balance equation reads

$$(F_{Aj}^{-1} \tau_{ij})_{,A} = 0, \quad \text{in } \Omega_0 \quad (1)$$

where τ_{ij} is the Kirchhoff stress tensor, $F_{jA} = x_{j,A}$ is the deformation gradient tensor and Ω_0 denotes the undeformed configuration. In the phase field method, the evolution of the phase field parameter c from 0 to 1 is used to track crack propagation. The parameter is 1 in the fully fractured phase and 0 in the undamaged phase. Crack evolution is assumed to be driven by micro forces [47], and governed by the following equation

$$H_{A,A} - K = 0, \quad (2)$$

where

$$H_A = \frac{\partial \Phi}{\partial c_{,A}} \quad (3)$$

is the microstress traction, which is work-conjugate to the flux $c_{,A}$, while

$$K = \frac{\partial \Phi}{\partial c} \quad (4)$$

is a micro force which is work-conjugate to c . Here, Φ is the total free energy of the system.

To specify the above balance equations, we assume a decomposition of the total free energy into a degraded elastic energy and a fracture energy part, as follows

$$\Phi = \Phi^{es} + \Phi_f, \quad (5)$$

where

$$\Phi^{es}(W_0) = W_0^- + m(c)W_0^+ \quad (6)$$

is a function of the elastic strain energy W_0 of an undamaged solid and the phase field parameter c . Here, W_0^- is the portion of the energy that is not degraded by fracture, while W_0^+ is the portion that is damaged due to fracture [40]. $m(c)$ is the degradation function that relates the phase-field parameter c with the damage in the material, which in this work is taken as

$$m(c) = (1 - c)^2. \quad (7)$$

The fracture energy is defined as [48,46]

$$\Phi_f = G_c \left(\frac{c^2}{4l_0} + l_0 c_{,A} c_{,A} \right). \quad (8)$$

Here, l_0 is the length scale employed to approximate the width of the crack process zone, while G_c is the fracture energy.

Substituting Eqs. (6) and (8) into Eq. (5), together with Eqs. (3) and (4), the micro force balance equation (2) can be rewritten as

$$c = 4l_0^2 c_{,AA} + \frac{2l_0}{G_c} \frac{\partial m(c)}{\partial c} W_0^+. \quad (9)$$

Together with the macro force balance equation (1), the strong form balance equations in the analysis domain Ω_0 can be summarized as

$$\begin{aligned} (F_{Aj}^{-1} \tau_{ij})_{,A} &= 0 && \text{in } \Omega_0 \\ c &= 4l_0^2 c_{,AA} + \frac{2l_0}{G_c} \frac{\partial m(c)}{\partial c} W_0^+ && \text{in } \Omega_0 \end{aligned} \quad (10)$$

with Neumann boundary conditions, or macro and micro traction conditions as

$$F_{Aj}^{-1} \tau_{ij} \cdot n_A^{\bar{T}} = \bar{T}_i \quad \text{in } \Gamma_0^{\bar{T}}, \quad (11)$$

$$c_{,A} \cdot n_A = 0 \quad \text{in } \Gamma_0. \quad (12)$$

Here, Γ_0 is the boundary of Ω_0 , $\Gamma_0^{\bar{T}}$ denotes the traction boundary. n_A is the unit normal to Γ_0 , and $n_A^{\bar{T}}$ is the unit normal to $\Gamma_0^{\bar{T}}$. The subscript 0 indicates the undeformed configuration.

Essential boundary conditions at the beginning of the loading are set to

$$u_i = \bar{u}_i \quad \text{on } \Gamma_0^u \quad (13)$$

where \bar{u}_i are prescribed displacements (fixed throughout the loading history).

Constitutive relations. In this work we consider natural rubber to be the matrix phase of the polymer composite, for which the Arruda–Boyce model [49] is employed. The standard elastic strain energy W_0 of the undamaged and weakly compressible Arruda–Boyce rubber material is partitioned into volumetric and deviatoric parts as [50]

$$W_0 = U(J) + \bar{W}(\bar{I}_1), \quad (14)$$

where

$$U(J) = \frac{K_m}{2} (\ln J)^2 \quad (15)$$

is the volumetric contribution [51]. Here, J denotes the determinant of the deformation gradient $J = \det(F_{iA})$, and $\bar{I}_1 = J^{-2/3} I_1$, where I_1 is the first invariant of the left Cauchy–Green tensor $b_{ij} = F_{iA} F_{jA}$. The bulk modulus K_m is given by $K_m = \frac{E}{3(1-2\mu)}$, where E is Young's Modulus, μ is Poisson's ratio, a subscript m is used to differentiate with the micro force work-conjugate K .

In the Arruda–Boyce model, the deviatoric contribution $\bar{W}(\bar{I}_1)$ takes the following form [52],

$$\bar{W}(\bar{I}_1) = C_1(\alpha_1(\bar{I}_1 - 3) + \alpha_2(\bar{I}_1^2 - 9) + \alpha_3(\bar{I}_1^3 - 27) + \alpha_4(\bar{I}_1^4 - 81) + \alpha_5(\bar{I}_1^5 - 243)) \quad (16)$$

where $C_1 = \frac{E}{2(1+\mu)}$ is the shear modulus, and α_1 – α_5 are scalars given by $\alpha_1 = \frac{1}{2}$, $\alpha_2 = \frac{1}{20\lambda_m^2}$, $\alpha_3 = \frac{11}{1050\lambda_m^4}$, $\alpha_4 = \frac{19}{7000\lambda_m^6}$, $\alpha_5 = \frac{519}{673750\lambda_m^8}$, where λ_m is the stretch at which the polymer chain network becomes locked. In the literature, C_1 and λ_m are generally found by curve fitting the experimental data.

As proposed by Miehe et al. [40], the undegraded free energy W_0 is further split to account for compression and tension such that

For tension ($J \geq 1$),

$$\begin{aligned} W_0^+ &= U(J) + \bar{W}(\bar{I}_1) \\ W_0^- &= 0. \end{aligned} \quad (17)$$

For compression ($J < 1$),

$$\begin{aligned} W_0^+ &= \bar{W}(\bar{I}_1) \\ W_0^- &= U(J). \end{aligned} \quad (18)$$

Based on a general hyperelastic potential form [53], one may write

$$\tau_{ij} = 2 \frac{\partial \Phi^{es}(b_{ij})}{\partial b_{ij}} b_{ij}, \quad (19)$$

where τ_{ij} is the Kirchhoff stress, while b_{ij} is the left Cauchy–Green strain tensor, both introduced earlier. Plugging Eqs. (17) and (18) into Eq. (6), together with the relation in Eq. (19), the following constitutive relationship is obtained

$$\tau_{ij} = \tau_{ij}^+ + \tau_{ij}^-, \quad (20)$$

where if $J \geq 1$,

$$\tau_{ij}^+ = m(c) \left(C_1 (2\alpha_1 + 4\alpha_2 \bar{b}_{kk} + 6\alpha_3 \bar{b}_{kk}^2 + 8\alpha_4 \bar{b}_{kk}^3 + 10\alpha_5 \bar{b}_{kk}^4) \left(\bar{b}_{ij} - \frac{1}{3} I_{ij} \bar{b}_{kk} \right) + K_m \ln J \delta_{ij} \right) \quad (21)$$

$$\tau_{ij}^- = 0 \quad (22)$$

while for $J < 1$,

$$\tau_{ij}^+ = m(c) C_1 (2\alpha_1 + 4\alpha_2 \bar{b}_{kk} + 6\alpha_3 \bar{b}_{kk}^2 + 8\alpha_4 \bar{b}_{kk}^3 + 10\alpha_5 \bar{b}_{kk}^4) \left(\bar{b}_{ij} - \frac{1}{3} I_{ij} \bar{b}_{kk} \right) \quad (23)$$

$$\tau_{ij}^- = K_m \ln J \delta_{ij}. \quad (24)$$

Here, $\bar{b}_{ij} = J^{-2/3} b_{ij}$.

2.2. The weak form

With the above balance equations and boundary conditions, the weak form is obtained in the usual way. Multiplying both equations by appropriate weight functions and integrating over the reference domain Ω_0 , one gets the weak form which correspond to finding $u \in \mathcal{S}_u$ and $c \in \mathcal{S}_c$ such that

$$\int_{\Omega_0} w_i^u (F_{Aj}^{-1} \tau_{ij})_{,A} d\Omega_0 - \int_{\Gamma_0^{\bar{T}}} w_i^u (F_{Aj}^{-1} \tau_{ij} \cdot n_A^{\bar{T}} - \bar{T}_i) d\Gamma_0^{\bar{T}} = 0, \quad \forall w^u \in \mathcal{W}_u, \quad (25)$$

$$\int_{\Omega_0} w^c \left(c - 4l_0^2 c_{,AA} + \frac{2l_0}{G_c} \frac{\partial m}{\partial c} W_0^+ \right) d\Omega_0 - \int_{\Gamma_0} w^c (c_{,A} \cdot n_A) d\Gamma_0 = 0, \quad \forall w^c \in \mathcal{W}_c \quad (26)$$

where the appropriate spaces are defined as follows,

$$\mathcal{S}_u = \{u(X) \mid u \in H^1, u = \bar{u} \text{ on } \Gamma^u\}; \quad \mathcal{S}_c = \{c(X) \mid c \in H^1\} \quad (27)$$

$$\mathcal{W}_u = \{w^u(X) \mid w^u \in H^1, w^u = 0 \text{ on } \Gamma^u\}; \quad \mathcal{W}_c = \{w^c(X) \mid w^c \in H^1\} \quad (28)$$

where H^1 is the Sobolev space of L_2 functions with square integrable derivatives. Integration by parts and application of the divergence theorem where appropriate, gives the following set of weak form equations

$$-\int_{\Omega_0} w_{i,A}^u F_{Aj}^{-1} \tau_{ij} d\Omega_0 + \int_{\Gamma_0^{\bar{T}}} w_i^u \bar{T}_i d\Gamma_0^{\bar{T}} = 0 \quad \forall w^u \in \mathcal{W}_u, \quad (29)$$

$$\int_{\Omega_0} \left(w^c \left(c + \frac{2l_0}{G_c} \frac{\partial m}{\partial c} W_0^+ \right) + 4l_0^2 w_{,A}^c c_{,A} \right) d\Omega_0 = 0 \quad \forall w^c \in \mathcal{W}_c. \quad (30)$$

2.3. Linearization and discretization of the weak form

Discretization of the weak form leads to a coupled nonlinear set of equations which in our work is solved simultaneously in a monolithic framework. To this end, we define a residual vector

$$\mathbf{R} = \begin{bmatrix} R^u & R^c \end{bmatrix}^T \quad (31)$$

following the weak form in Eqs. (29) and (30), where the residuals of the macro and micro equilibrium equations are given as

$$R^u = -\int_{\Omega_0} w_{i,A}^u F_{Aj}^{-1} \tau_{ij} d\Omega_0 + \int_{\Gamma_0^{\bar{T}}} w_i^u \bar{T}_i d\Gamma_0^{\bar{T}}, \quad (32)$$

$$R^c = \int_{\Omega_0} \left(w^c \left(c + \frac{2l_0}{G_c} \frac{\partial m}{\partial c} W_0^+ \right) + 4l_0^2 w_{,A}^c c_{,A} \right) d\Omega_0. \quad (33)$$

Linearization of the PDE system is obtained by differentiating the weak form of the residuals (32) and (33), and substituting the Galerkin approximation for the displacements and phase field parameter. For a single element, the Galerkin approximation reads

$$\begin{aligned} u_i &= N_{i\alpha}^u \cdot \hat{u}_\alpha; & w_i^u &= N_{i\alpha}^u \cdot \hat{w}_\alpha^u; & \alpha &= 1, \dots, 8, i = 1, 2 \\ c &= N_\psi^c \cdot \hat{c}_\psi; & w^c &= N_\psi^c \cdot \hat{w}_\psi^c; & \psi &= 1, \dots, 4 \end{aligned} \quad (34)$$

and where N is a tensor containing the appropriate element shape functions and defined in undeformed configuration. In this work, we employ standard bilinear functions for both displacements and the phase field parameter. The hatted field variables are nodal degrees of freedom belonging to a single element.

In a monolithic framework, the coupled, nonlinear residual equations are solved simultaneously until convergence. In the current work, we employ a Newton type method where at every nonlinear iteration k a linear solution of the Jacobian (or tangent stiffness) matrix is required. To this end, we employ the Gâteaux derivative approach in which the product of the Jacobian \mathbf{J} is the directional derivative of the residual \mathbf{R} with respect to the variation $\delta\mathbf{p}^k$, and is defined in finite difference form as

$$\mathbf{J}\delta\mathbf{p} = \delta\mathbf{R}\left[\delta\mathbf{p}^k\right] = \lim_{\varepsilon \rightarrow 0} \frac{1}{\varepsilon} \left(\mathbf{R}\left[\mathbf{p}^k + \varepsilon\delta\mathbf{p}\right] - \mathbf{R}\left[\mathbf{p}^k\right] \right) = \frac{d}{d\varepsilon} \mathbf{R}\left[\mathbf{p}^k + \varepsilon\delta\mathbf{p}\right] \Big|_{\varepsilon=0} \quad (35)$$

where

$$\mathbf{p} = \begin{bmatrix} u_i & c \end{bmatrix}^T. \quad (36)$$

This derivative can be computed analytically without numerical differentiation in blocks to get the fully discrete Jacobian. In such monolithic framework, the linearized system can be written in a partitioned form as follows

$$\begin{bmatrix} \mathbf{L}_{\alpha\beta}^{uu} + \mathbf{G}_{\alpha\beta}^{uu} & \mathbf{C}_{\alpha\kappa}^{uc} \\ \mathbf{W}_{\psi\beta}^{cu} & \mathbf{M}_{\psi\kappa}^{cc} + \mathbf{K}_{\psi\kappa}^{cc} \end{bmatrix}^k \begin{bmatrix} \delta\hat{u}_\beta \\ \delta\hat{c}_\kappa \end{bmatrix} + \begin{bmatrix} R_\alpha^u \\ R_\psi^c \end{bmatrix}^k = \mathbf{0}, \quad (37)$$

where,

$$\mathbf{L}_{\alpha\beta}^{uu} = - \int_{\Omega_0} N_{i\alpha,A}^u F_{Aj}^{-1} \tau_{il} \delta_{jk} N_{k\beta,B}^u F_{Bl}^{-1} d\Omega_0 \quad (38)$$

is a term that arises from geometric nonlinearity, and

$$\mathbf{G}_{\alpha\beta}^{uu} = \int_{\Omega_0} N_{i\alpha,A}^u F_{Aj}^{-1} \left(\delta\tau_{ik} [\delta u_h] \right) \delta_{lj} N_{k\beta,B}^u F_{Bl}^{-1} d\Omega_0 \quad (39)$$

is due to material nonlinearity. Here, $\delta\tau_{ik} [\delta u_h]$ is the variation of τ_{ik} with respect to displacement u_h .

$$\mathbf{C}_{\alpha\kappa}^{uc} = \int_{\Omega_0} N_{i\alpha,A}^u F_{Aj}^{-1} \left(\delta\tau_{ij} [\delta c] \right) N_\kappa^c d\Omega_0 \quad (40)$$

arises from the derivative of the degradation function $m(c)$ with respect to the phase field parameter c . $\delta\tau_{ij} [\delta c]$ is the variation of τ_{ij} with respect to phase field parameter c .

$$\mathbf{W}_{\psi\beta}^{cu} = \int_{\Omega_0} N_\psi^c \frac{2l_0}{G_c} \frac{\partial m}{\partial c} \delta W_0^+ [\delta u_h] N_{i\beta,A}^u d\Omega_0 \quad (41)$$

comes from the linearization of W_0^+ with respect to displacement \mathbf{u} . $\delta W_0^+ [\delta u_h]$ is the variation of W_0^+ with respect to displacement u_h .

$$\mathbf{M}_{\psi\kappa}^{cc} = \int_{\Omega_0} N_\psi^c \left(1 + \frac{2l_0}{G_c} \frac{\partial^2 m}{\partial c^2} W_0^+ \right) N_\kappa^c d\Omega_0 \quad (42)$$

is the mass matrix term corresponding to the phase field evolution equation.

$$\mathbf{K}_{\psi\kappa}^c = \int_{\Omega_0} N_{\psi,A}^c 4l_0^2 N_{\kappa,A}^c d\Omega_0 \quad (43)$$

is a stiffness matrix that arises from the Laplacian term in Eq. (9). Detailed derivations of these terms can be found in the [Appendix](#).

3. Validation examples and modeling assumptions

The hyperelastic Arruda–Boyce model coupled with the phase field method is validated first on a double-edge notched specimen in tension for which experimental data are available. Then, the performance of the model is illustrated on two examples with low and high stiff inclusions, and the assumptions and limitations of the model are outlined.

3.1. Double-edge notched specimen in tension

The model is validated by a boundary value problem with experimental data available in Hocine et al. [54]. The experiments reported are performed on double-edge notch tension specimens to estimate the critical fracture energy. The geometry of the model is shown in [Fig. 2](#), where all dimensions are given in mm. Five different initial crack length a are considered as follows: $a_i = [12, 16, 20, 24, 28]$ mm. The Young's modulus of rubber is assumed to be 1.95 MPa and its Poisson ratio 0.45. The parameter λ_m^2 is selected as 25.9. In our simulation, we exploit the symmetry of the problem and consider only one quarter of the specimen. The critical fracture energy G_c is 0.36 N/mm. Here, we define the stretch of the specimen λ as the amount of deformation the rubber experienced during the deformation

$$\lambda = \frac{l}{L}, \quad (44)$$

where L is the original length in the tension direction of the plate, and l is the current length.

First, a benchmark problem with $a = 28$ mm is meshed and the area where the crack is expected to propagate is refined with an effective element size of 2 mm (2512 elements), 2.5 mm (2488 elements) and 3 mm (2236 elements), respectively, to study the mesh sensitivity of the model. The phase field length scale is taken to be $l_0 = 6$ mm. The results of this study are shown in [Fig. 3](#). Only minor differences between the 3 different meshes can be observed, which confirms that the model is not sensitive to the mesh size.

Next, the five different geometry configurations of the model shown in [Fig. 2](#) are calculated with the above material parameter combination and an effective element size of 2 mm. The resulting force–displacements curves are plotted and displayed. The results and the experimental results of Hocine et al. [54] are shown in [Fig. 4](#). Overall, good agreement with the experimental data reported in the literature is obtained.

Furthermore, it can be seen that the specimen with the 12 mm notches undergoes the largest stretch and the corresponding peak force is also the largest, while the specimen with the 28 mm notches undergoes the smallest stretch and the corresponding peak force is the smallest. The crack propagation path for $a = 12$ mm is illustrated in the snapshots shown in [Fig. 5](#).

3.2. Double-edge notched rubber reinforced by carbon black particles

The second example, shown in [Fig. 6](#), is the analysis of a double-edge notched rubber reinforced by carbon black particles. Due to the lack of experimental results, the key idea here is to illustrate the behavior and model response under the modeling assumptions of the rubber with particles before proceeding to the Monte Carlo simulations. To reveal, to some extent, the interaction between crack propagation path and the polymer composite microstructure, we analyze an example with one large central particle and 2 large cut edged particles on the boundaries. In this example, the length of the notch is set equal to 0.11 mm and the particles radius is set equal to 0.218 mm in order to obtain a volume fraction of $\nu = 30\%$.

As before, the same loading and boundary conditions are applied and the rubber is modeled by the Arruda–Boyce hyperelastic model, while the stiff particles are modeled with a Neo-Hookean hyperelastic model. The material

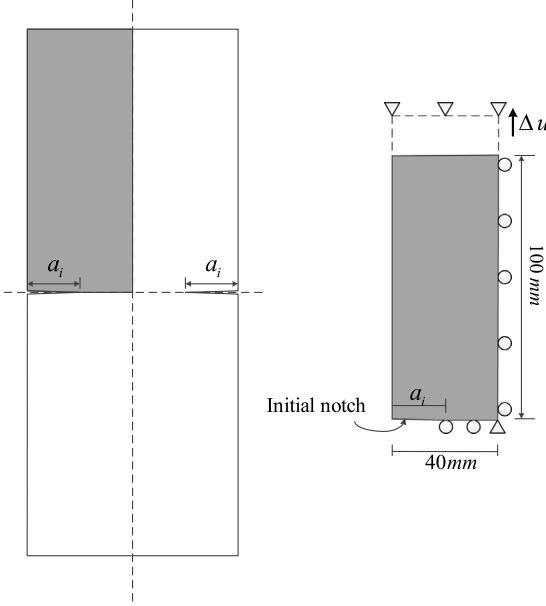


Fig. 2. Boundary conditions and geometry of the benchmark example with double-edge notches.

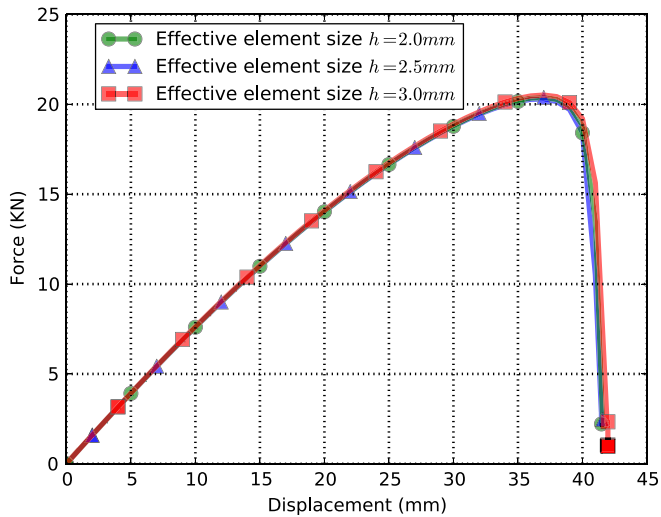


Fig. 3. Mesh sensitivity study. Force–displacement curves with varying mesh sizes obtained for a double-edge notch specimen with $a = 28$ mm in tension.

parameters adopted in this example are given in Table 1. The effective element size $h = 0.02$ mm and 5245 finite elements are used for spatial discretization. We assume perfect bounding between CB particles and the NR matrix, which means that fracture would not develop at the interface rubber/inclusion and our model does not take into account de-cohesion effects.

The result illustrating several snapshots of the rupture of rubber with stiff CB circular particles is shown in Fig. 7. With the increase in stretch, voids are initiated at several areas simultaneously: above and below the middle particle and close to the notch tips, as shown in Fig. 7(b). These voids propagate and finally merge to form a curved crack path as observed in Fig. 7(e).

The analysis is repeated for the very stiff inclusions and the corresponding rubber rupture is shown by the snapshots in Fig. 8. Similarly, voids are formed simultaneously at the same locations as before. However, the material

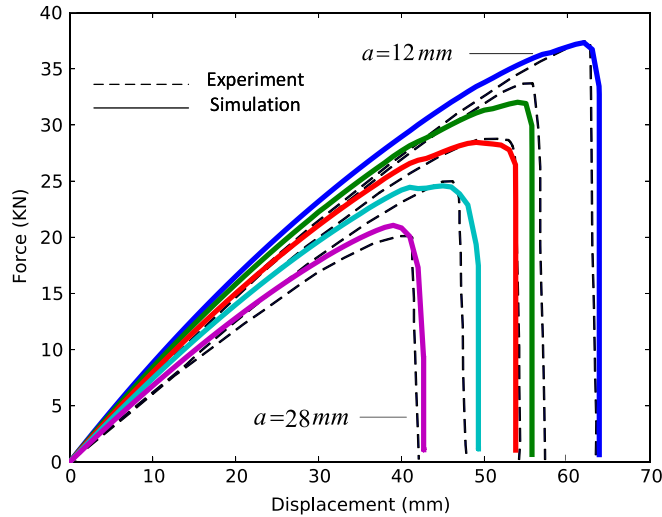


Fig. 4. Validation studies. Force–displacement curves with varying notch length of 12, 16, 20, 24, 28 mm for a double-edge notch specimen in tension.

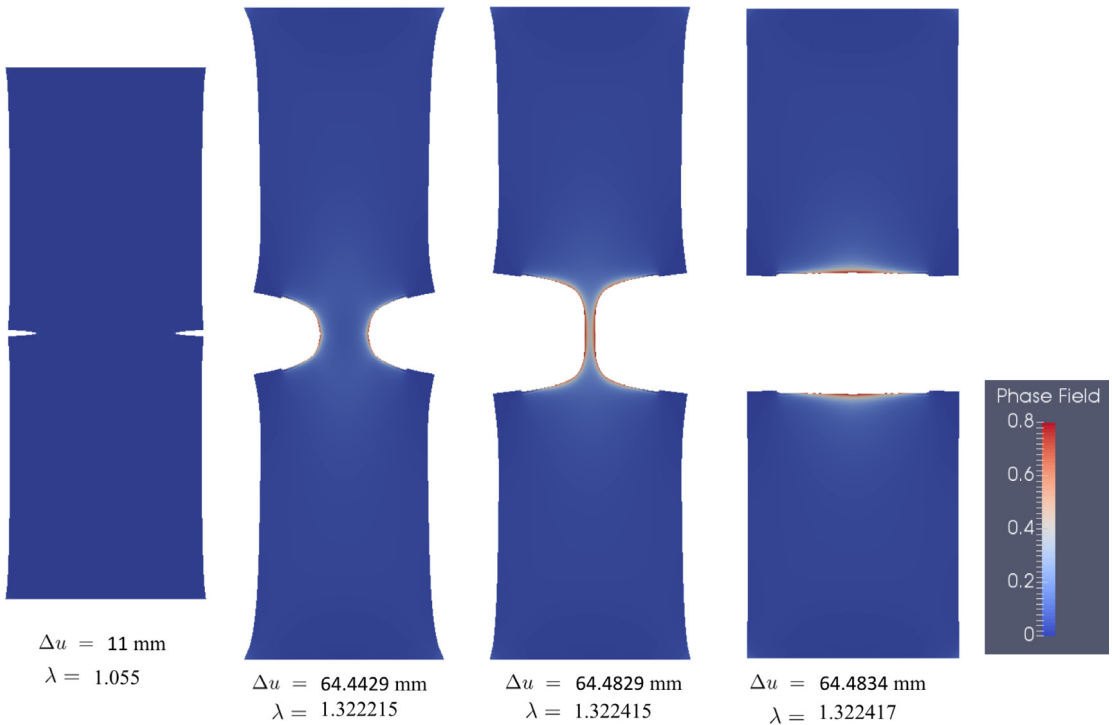


Fig. 5. Snapshots depicting the rupture of a double edge notch specimen with initial notch length of $a = 12\text{ mm}$, as a function of increased displacement in the vertical direction. The values of displacement and stretch are indicated. For illustration purposes, elements with a phase field value of $c > 0.8$ have been removed.

degradation at the notch tips area is not evident. In other words, the voids that form in between the particles are more significant and one of the voids continues to propagate in a straight line (corresponding to a mode I fracture) until the specimen is completely ruptured.

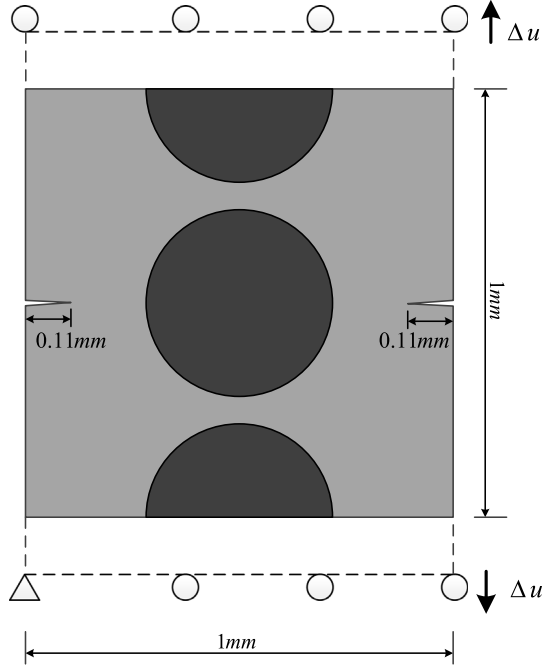


Fig. 6. Geometry and boundary conditions of the second validation example. The length of the notch is 0.11 mm. The radius of the 3 circular particles is 0.218 mm, which makes the volume fraction $\nu = 30\%$.

Table 1
Material parameters.

Material	Constitutive model	Model parameters
Rubber matrix	Arruda–Boyce	$E = 13.5 \text{ MPa}$, $\mu = 0.45$ $\lambda_m^2 = 25.9$
Stiff CB particles	Neo-Hookean	$E = 1350 \text{ MPa}$, $\mu = 0.3$
Very stiff CB particles	Neo-Hookean	$E = 135\,000 \text{ MPa}$, $\mu = 0.3$
Phase field parameters		$l_0 = 0.1 \text{ mm}$, $G_c = 0.28 \text{ N/mm}$

4. Monte Carlo approach

To quantify the uncertainty in the rupture of CB reinforced NR, a Monte Carlo (MC) simulation approach is carried out with random elliptical particles. In this section, we outline the steps involved with the MC implementation, as follows:

- Given a fixed volume fraction ν and number of particles np , sample realizations of the random distribution for particle size, position and orientation are generated.
- Each realization undergoes large stretching up to failure, and force–displacement curves, stretches and fracture energies are recorded. Failure of a sample is defined as the point where the load drops to 75% of its peak value.
- The statistics of the MC analysis is assembled and the distribution of fracture properties including peak force, failure stretch and fracture energy are plotted and compared for different volume fractions ν .

4.1. Generation of sample realizations

With reference to the work of Koga et al. [55], CB fillers in a rubber matrix could be understood in different hierarchical structures as illustrated in Figure 13 in that paper. In structure level 1, CB diameter ranges from a few tens to a few hundred nanometers. However, when those particles agglomerate they form larger macro particles and are denoted as a level 2 structure. Correspondingly, in our Monte Carlo simulation, we consider these

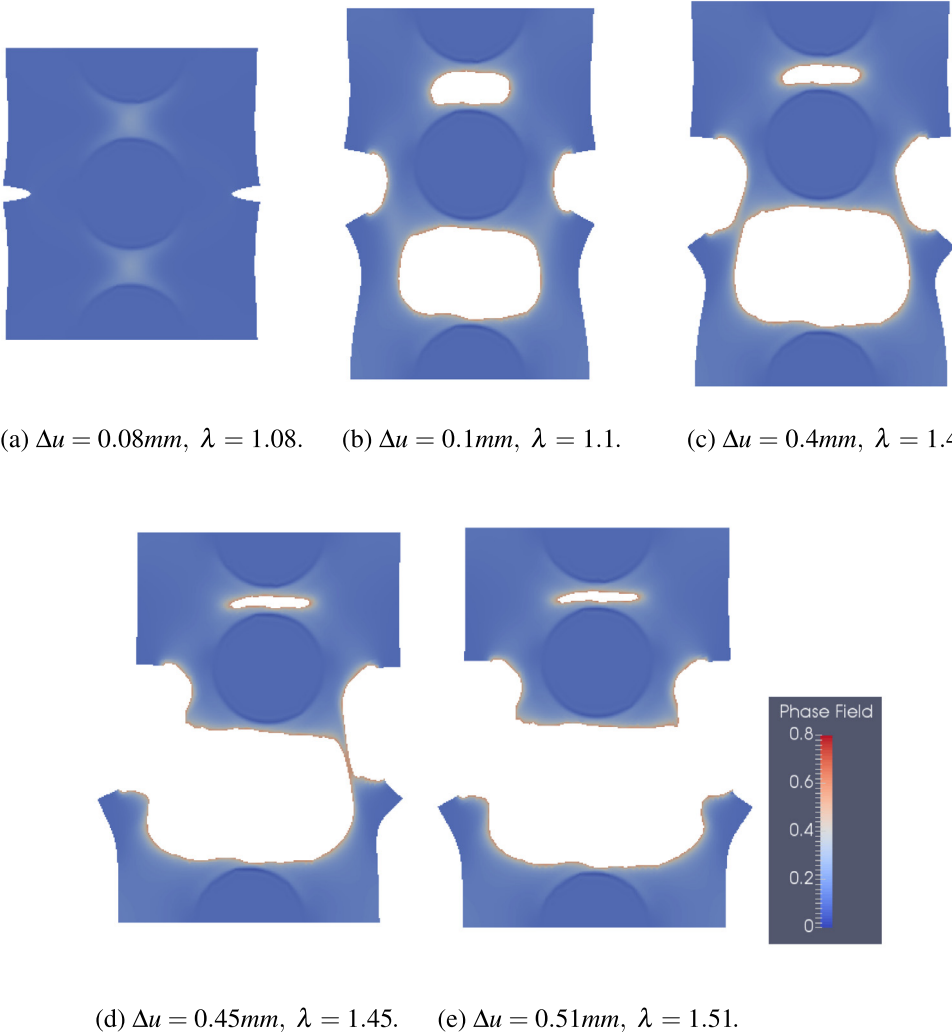


Fig. 7. Snapshots showing the rupture of a double-edge notched natural rubber reinforced by stiff carbon black particles.

agglomerated particles and generate sample realizations based on a level 2 structure. The agglomerated CB particles are approximated as elliptical particles with random shapes and orientations.

Many algorithms have been developed for random generation of elliptical particles in a unit cell, see for example [33,34]. However, in these algorithms, particles were not present on the boundaries or at the corners of the cell. While this may be adequate for the analysis of homogenized elastic properties of a composite, it is not suitable for hyperelastic rupture analysis since cracks may always initiate and propagate along the boundaries in which case the stochastic analysis will be biased and unrepresentative.

To eliminate this bias, a new algorithm that allows particles to be placed at boundaries and corners is developed to generate the realizations for the MC simulation. In this new algorithm, elliptical particles cut by the boundaries appear on the opposite edge, as a mirror image. Same rules are also applied to a particle at the corner and hence the remainder of this particle will be mirrored to the remaining three corners.

We start by first defining a unit cell with edge length parameters x_{len} and y_{len} along x and y directions, respectively. The major and minor radii of an elliptical particle, A and B respectively, their aspect ratio $r = B/A$, the particle position at point C and its orientation θ with respect to the horizontal axis, are illustrated in Fig. 9. Four independent probability distributions, denoted as f_c , f_θ , f_r , and f_A , are defined for generation of MC realizations.

The first two, f_c and f_θ , model the coordinates of the center C of the elliptical particle and its orientation angle θ , respectively. Both follow the uniform distribution over the intervals $[0, 1]$ and $[-\pi, \pi]$, respectively (note that the

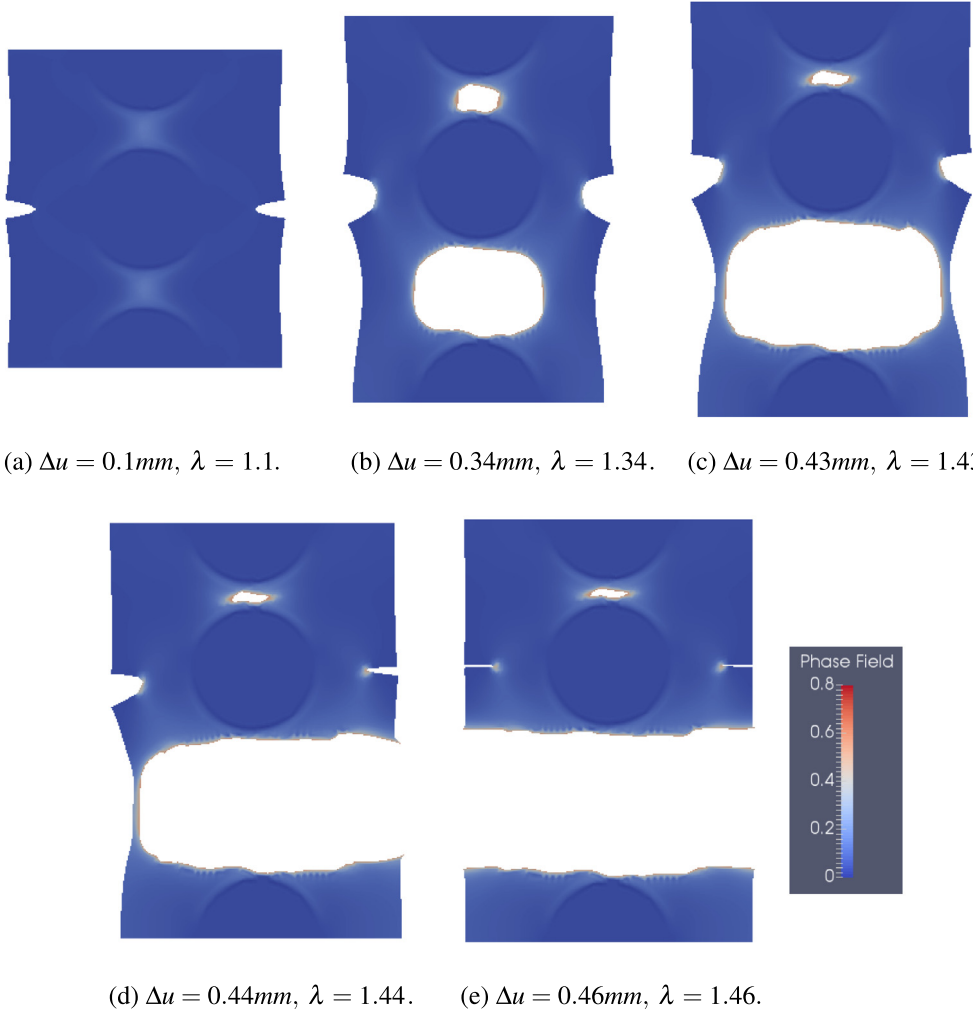


Fig. 8. Snapshots showing the rupture of a double edge notched natural rubber reinforced by very stiff carbon black particles.

x and y coordinates of point C are generated separately). f_r models the aspect ratio r between the minor radius and the major radius, and follows a uniform distribution in the range [0.7, 0.9] to avoid too narrow elliptical particles. Finally, the uniform distribution is also used to model the major radius f_A in the range [0.6, 0.8] to avoid too large size variations between elliptical particles. For elliptical particles cut by a boundary, we define the distance ratio r_d as the ratio between the distance d from the boundary and the minor radius B , as illustrated in Fig. 9. The distance ratio r_d is set to be less than 0.3 in order to avoid the remainder of the cutoff particle to be too narrow.

In addition, for the generation of the finite element mesh, one has to impose that particles are not overlapping. The shortest distance between two adjacent elliptical particles V_d is defined, as shown in Fig. 10. In our simulations, we set $V_d = 0.05 \times \sqrt{x_{len} \times y_{len}}$, considering that the element size h is about $0.02 \times \sqrt{x_{len} \times y_{len}}$.

The criterion to check whether the elliptical particles overlap is given by

$$D > 2 \times A_{i2} + 2 \times A_{ip} + 2 \times V_d, \quad (45)$$

as illustrated in Fig. 10. Here, D is the sum distance of the foci of two adjacent elliptical particles: $D = D_1 + D_2$.

The procedure to perform the Monte Carlo simulation is described in Algorithm 1. Note that all parameters employed in the algorithm are summarized in Table 2, including their values or ranges chosen in this work.

Algorithm 1: Generation of sample realizations with randomly distributed elliptical particles

```

1 Input  $v, np, ip, i2, xlen, ylen, f_c, f_\theta, f_A, f_r$ . The definitions and values of these variables are provided in
Table 2
2 Generate / Sort / Scale elliptical particles:
3 Generate the vector  $AA$  for  $np$  elliptical particles in accordance to  $f_A$ , and sort it in descending order
4 Generate the vector  $RR$  for  $np$  elliptical particles in accordance to  $f_r$ 
5 Calculate the vector  $BB$  for  $np$  elliptical particles, and calculate scalar for the sum of particle areas with
reference to the volume fraction:  $scaler = \sqrt{v \times xlen \times ylen / (\pi \times AA^T \cdot BB)}$ 
6 Scale the vector  $AA$  to fit the volume fraction  $v$ :  $AA_s = AA \times scaler$ 
7 Spatially distribute the elliptical particles within a unit cell:
8  $ip = 1$ 
9 while  $ip \leq np$  do
10   Generate the center coordinates and orientation angle for elliptical particle  $ip$ ;
11   if  $D > 2 \times AA_s(i2) + 2 \times AA_s(ip) + 2 \times V_d$  then
12     if elliptical particle ip is cut by boundary edge(s) then
13       if  $r_d < 0.3$  then
14         | Record the intersection point;
15       end
16     end
17     Record the center coordinates, the orientation angle, the major and minor radii of particle  $ip$ ;
18      $ip = ip + 1$ ;
19   end
20 end

```

4.2. Results of MC analysis

The critical fracture energy of CB reinforced NR will be affected significantly by the interaction between the particles and the matrix. The critical fracture energy varies with the heterogeneous composition parameters including the volume fraction v , the stiffness ratio R_E between particles and matrix, as well as the particle size, shape, orientation and spatial distribution.

In general, the larger the number of realizations in the MC simulation, the more accurate the acquired results will be. Nonetheless, a very large number of realizations leads to a major computational burden. Hence, there should be a balance between accuracy and computational effort. To this end, a criterion is developed to determine the number of realizations necessary before terminating the MC simulation. The criterion is based on the convergence of the mean value of the cumulative peak force which is monitored during the simulations. In addition, the coefficient of variation of the last 100 computed mean values of the cumulative peak force, denoted by CV_{100} , is calculated and the MC simulation is terminated when CV_{100} becomes less than 0.05%. The calculation of the mean value of the cumulative peak force F^{ac} is given as

$$F_i^{ac} = \frac{\sum_{i=1}^n F_i^{peak}}{n}, \quad i = 1, 2, 3, \dots, n, \quad (46)$$

while the value of CV_{100} is obtained from the following expression:

$$CV_{100} = \max \left(\left| \frac{F_i^{ac} - F_n^{ac}}{F_n^{ac}} \right| \right), \quad i = n - 99, n - 98, \dots, n, \quad (47)$$

where n is the total number of simulated realizations.

In order to get insight into the behavior of CB reinforced NR, we define two sets of parameters. The first parameter set is related to the deformation state at which the peak force occurs: the peak force F^{peak} , the corresponding stretch λ_f^{peak} and the corresponding fracture energy Φ_f^{peak} . The second parameter set is related with the failure state point

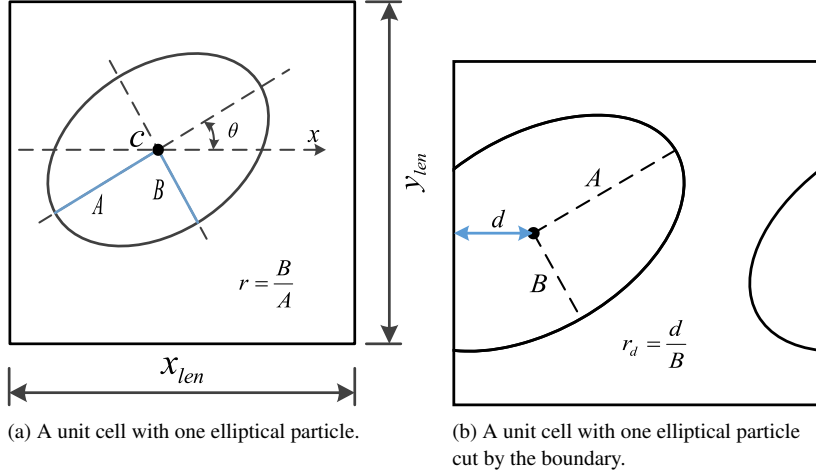


Fig. 9. Parameters used to generate elliptical particles in Algorithm 1. A and B are the major and minor radii, respectively. C is the center of the ellipse, θ is the orientation angle, and r is the aspect ratio. d is the distance between the center of the elliptical particle and the unit cell boundary. r_d is the ratio between d and B .

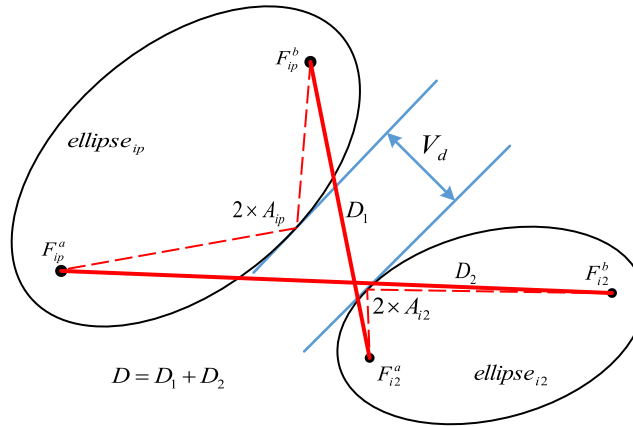


Fig. 10. Criterion used to ensure non-overlapping elliptical particles. ip and $i2$ indicate two adjacent elliptical particles. F indicates the two foci of an elliptical particle. D is the sum distance of the foci of the two elliptical particles. A_{ip} and A_{i2} are the major radii A of the elliptical particles ip and $i2$, respectively. V_d is the shortest distance between elliptical particles ip and $i2$. These parameters are used in Algorithm 1.

which is defined as: the force at 75% of its peak value F^{75} , the corresponding stretch λ_f^{75} , and the corresponding fracture energy Φ_f^{75} .

The definition of the fracture energy, computed based on the phase field parameter, is given in Eq. (8). While the actual crack pattern in the composite due to stretching and large deformations is very complex, the fracture energy gives a single scalar quantity that represents the energy that has been dissipated by nucleation and propagation of fracture surfaces, and therefore provides an excellent measure of the extent of damage in the specimen. With these definitions, the relationship between the volume fraction ν and these failure parameters can be investigated through the MC simulations.

5. Numerical examples

A rigorous stochastic analysis, employing the phase field method for fracture, is carried out to study the degradation, cracking and failure of reinforced natural rubber from stretching. Three sets of studies are considered in this Section. The first set includes a pre-notched sample with distributed voids within the rubber, with damage and

Table 2

Input variables for Algorithm 1.

Parameter definition	Symbol	Value
Volume fraction	ν	10%–30%
Number of elliptical particles	np	30
Index for current elliptical particle	ip	$1, 2, 3, \dots, np$
Index for previously generated elliptical particle	$i2$	$0, 1, 2, \dots, np - 1$
Length of the rubber matrix side in x direction	x_{len}	1
Length of the rubber matrix side in y direction	y_{len}	1
Uniform distribution for major radius	f_A	[0.6, 0.8]
Uniform distribution for aspect ratio	f_r	[0.7, 0.9]
Uniform distribution for central coordinates of point C	f_c	[0.0, 1.0]
Uniform distribution for orientation angle	f_θ	$[-\pi, \pi]$
Major radius of an elliptical particle	A	Random value defined by f_A and scaled by ν
Aspect ratio of an elliptical particle	r	Random value defined by f_r
Minor radius of an elliptical particle	B	$B = A \times r$
Coordinates of center of an elliptical particle	C	Random value defined by f_c
Orientation angle of an elliptical particle	θ	Random value defined by f_θ
AA , BB , and RR : arrays with np stored values for the major radius A , minor radius B , and aspect ratio r , respectively.		

cracks initiated at the notch tip. The second and third sets involve intact rubber samples with inclusions where cracks form at arbitrary locations and propagate within the matrix. In the second case we consider a low inclusion/rubber stiffness ratio, while in the third case a high ratio is considered. For each case studied, a statistical analysis is carried out to provide insight into the rupture of the composite.

In the MC simulations, a 30%–50% stretch is observed before the failure of every sample realization. A large deformation, coupled hyperelastic-phase field quad element has been implemented as a user element in the finite element code FEAP [56]. Finite element meshes are generated using gmsh [57], and ParaView [58] and Matplotlib [59] are used to visualize the results.

The linear problem shown in Eq. (37) is assembled using PETSc version 3.5.4 [60] and solved using the PETSc interface to UMFPACK [61], a sparse direct solver.

The material parameters used in this MC simulation are shown in Table 1. The phase field length scale l_0 used in the MC simulation is 0.1 mm, while the effective element size of the finite element mesh is 0.02 mm. The total number of the elements is on average 2500.

The number of samples in all following MC simulations is selected to provide accurate estimation of the mean values according to the criterion described in Section 4.2. For the selected number of samples, histograms and corresponding standard derivations are provided. However, the number of samples used is not large enough for accurate estimation of probability distributions. Histograms and standard derivations are provided to demonstrate qualitative behavior. The computational burden for accurate estimation of probability distributions is prohibitive.

5.1. Case 1: pre-notched samples with voids

The first case study includes NR under stretching with arbitrary distributed voids and pre-notches. Pre-notches are employed in this example in order to initiate cracks at a controlled location: the notch tips. The parameters used for the NR and phase field are summarized in Table 1. Volume fraction of voids ν is set to take the following values: 10%, 15% and 20%.

A representative realization with volume fraction 15% can be seen in Fig. 11. The dimensions of the unit cell are taken as 2 mm by 1 mm. Two notches are placed at the center of the edges with length of 0.5 mm having a small opening of $\delta = 0.01$ mm. These relatively long and sharp cracks are used to initiate and propagate the cracks. A displacement control approach is used to incrementally displace the specimen in tension, by increments of Δu , until the rubber ruptures. The corresponding snapshots of its stretching up to the rupture point are shown in Fig. 12.

As shown in the snapshots in Fig. 12(a)–(f), damage is initiated and forms cracks that propagate in a complex pattern that eventually connects the two notches and goes through narrow strips in between voids. In fact, under these

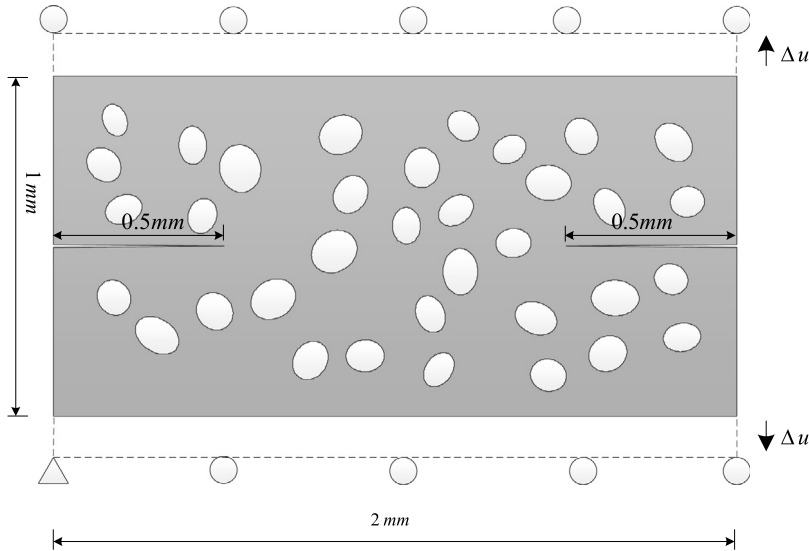


Fig. 11. Geometry and boundary conditions of the pre-notched natural rubber sample for one representative MC realization with elliptical voids at a volume fraction of $v = 15\%$. Δu refers to a displacement control approach used to incrementally stretch the sample until its rupture.

large deformation settings, cracks may initiate at several locations simultaneously and propagate until a macro crack is obtained.

This is in contrast with the case study shown in [44], where a crack propagation path is approximately a straight line connecting the two tips. While in our study the crack path is not the shortest path between the two notch tips, it is the optimal one, in a local sense at a given point in terms of energy dissipation.

The force–displacement curve and the fracture energy–displacement curve of the sample realization shown in Fig. 11, are shown in Figs. 13(a) and 13(b), respectively. The peak and failure quantities defined earlier in the paper: F^{peak} , λ_f^{peak} , Φ_f^{peak} , F^{75} , λ_f^{75} and Φ_f^{75} are marked on these plots.

The peak force is obtained as $F^{peak} = 1.209$ kN and 75% of its peak value is $F^{75} = 0.907$ kN. The stretch at the peak point is $\lambda_f^{peak} = 1.310$ and the stretch at the failure point $\lambda_f^{75} = 1.401$.

It should be noted that the fracture energy at the peak point is just $\Phi_f^{peak} = 0.024$ J, but is boosted to $\Phi_f^{75} = 0.107$ J at failure, which means that most of the material degradation happens after the peak force is reached.

The results of the MC simulations are reported in Figs. 14–16 for the different volume fractions of 10%, 15% and 20%. In all of these plots, Figure (a) shows the evaluation of the average cumulative peak force versus the current realization number. The evaluation of the average cumulative failure stretch is given in (b), and the same curve for fracture energy is shown in (c).

The peak force for every realization and its corresponding histogram is shown in Figure (d). Figure (e) shows the values for the failure stretch of the specimen and the corresponding histogram. Figure (f) shows the values for the fracture energy and the corresponding histogram.

From Figs. 14–16(a) and (d), it can be seen that the values of F^{peak} and F^{75} have the same standard deviation, σ but different mean value, μ_m values. This is an expected result since F^{75} is computed directly from the peak value. However, the distributions for the peak and failure stretches λ_f^{peak} and λ_f^{75} , respectively, and for the peak and failure fracture energies Φ_f^{peak} and Φ_f^{75} , respectively, are different. For example, as seen in Fig. 14(e), the σ value of λ_f^{peak} is 0.017, while it is 0.018 for λ_f^{75} . The σ value of Φ_f^{peak} is 0.007, but increases to 0.016 at failure. Hence, the uncertainty clearly increases at failure. The same trend is observed for all three volume fractions considered.

The results from all three volume fractions are summarized in Fig. 17 where the variations of the peak force, failure stretch and fracture energy are provided. As the volume fraction of voids increases, the peak force average and the failure force average drop dramatically (see Figs. 17(a) and 17(b)), while the peak and failure stretch average remain essentially constant (see Figs. 17(c) and 17(d)), and the fracture energy is decreasing only slightly (see Figs. 17(e) and 17(f)).

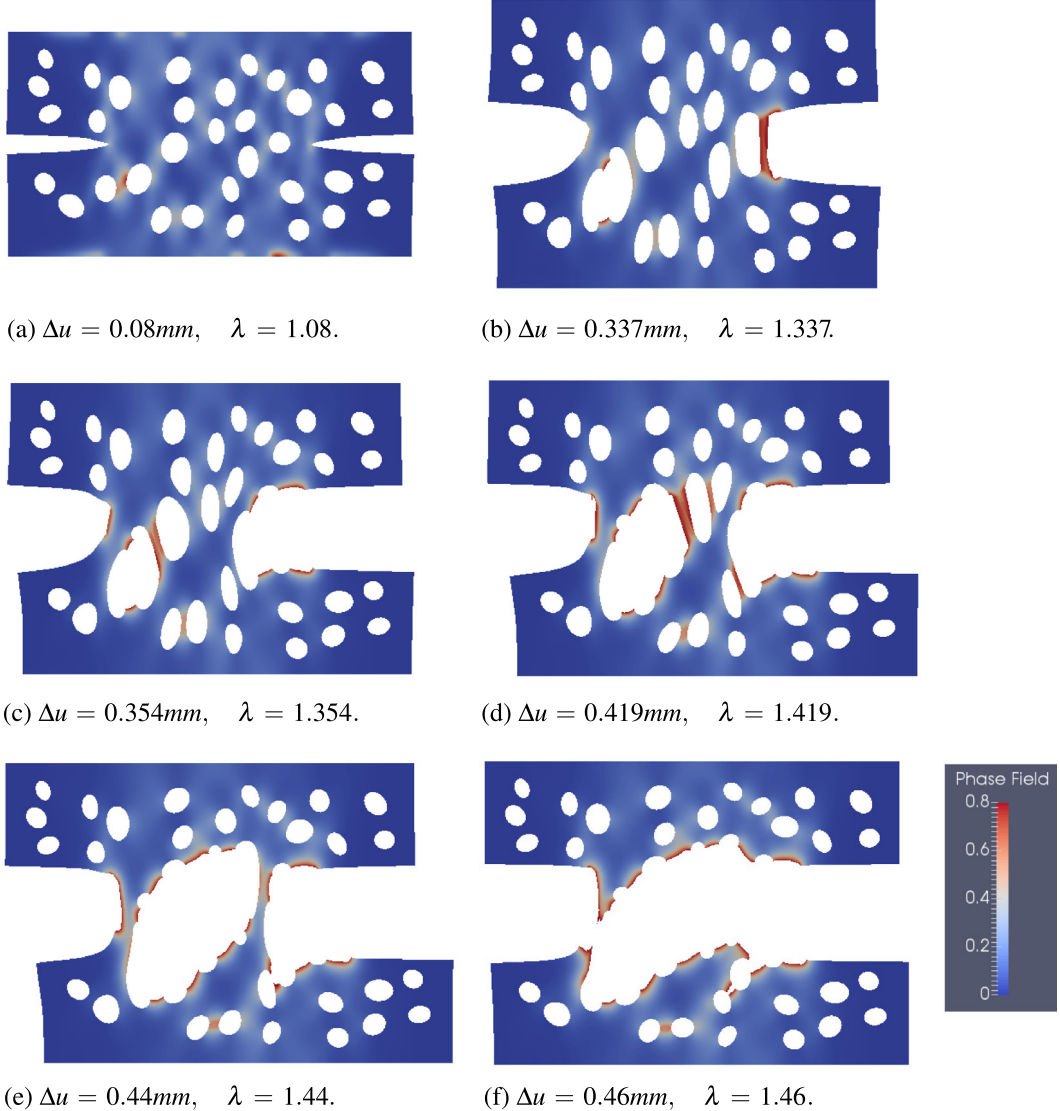


Fig. 12. Snapshots showing the complex crack propagation topology for the sample realization in Fig. 11 due to large deformation stretching.

5.2. Case 2: samples with low inclusion/matrix stiffness ratio

In the second set of MC samples, the NB is reinforced with stiff CB particles. The parameters used for rubber, stiff particles and phase field are summarized in Table 1. The volume fraction of CB inclusions in this set takes the following values: 10%, 20% and 30%. With reference to [55], the radii of CB inclusions range between 20 and 55 μm . Correspondingly, we choose 35 CB inclusions per sample realization.

A representative realization with volume fraction 30% is shown in Figs. 18 and 19. The dimensions of the unit cell are taken as 1 mm by 1 mm. It can be seen that damage is initiated and cavities are formed between some elliptical particles. These cavities coalesce until a macro crack is formed. This is qualitatively in agreement with the experimental results of [4] which is schematically illustrated in Fig. 1. With the incremental increase of the displacement by Δu , the macro crack propagates by bypassing stiff inclusions and approximately along a path vertical to the load direction (overall in a mode I propagation).

The force-displacement curve and the fracture energy-displacement curve of the sample realization are shown in Fig. 20(a), and Fig. 20(b), respectively. The peak and failure quantities defined earlier in the paper: F^{peak} , λ_f^{peak} ,

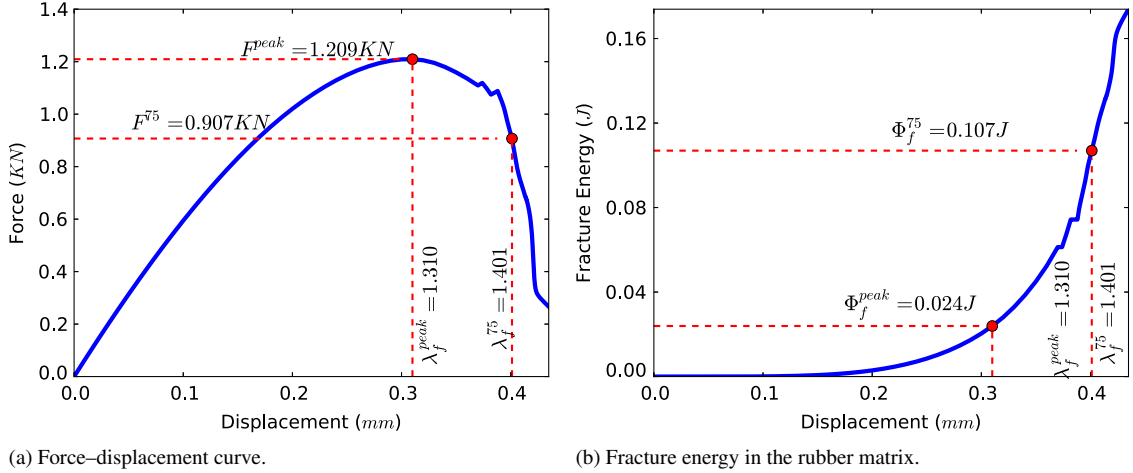


Fig. 13. Results for the sample in Figs. 11 and 12.

Φ_f^{peak} , F^{75} , λ_f^{75} and Φ_f^{75} are marked on these plots. Comparing the results shown in Figs. 13 and 20, the reinforcement effect of the CB particles is notable. The value of F^{peak} increases from 1.209 to 3.713 kN, and the value of F^{75} increases from 0.907 to 2.785 kN. However, the reinforcement of CB reduces the stretch λ_f^{peak} from 1.310 to 1.230, and decrease the value of λ_f^{75} from 1.401 to 1.387. A significant increase due to the CB reinforcement can be observed in the fracture energy curve. The value of Φ_f^{peak} increases from 0.024 J to 0.086 J, and Φ_f^{75} increases from 0.107 J to 0.493 J. Also by comparing the values of Φ_f^{peak} and Φ_f^{75} in this case, one can observe that a significant material degradation occurs after softening begins.

The results of the MC simulations are reported in Figs. 21–23 for different volume fractions of 10%, 20% and 30%. In all of these plots, Figure (a) shows the evaluation of the average cumulative peak force versus the current realization number. The evaluation of the average cumulative failure stretch and of the average cumulative fracture energy is given in (b) and (c), respectively.

The peak force for every realization and its corresponding histogram is shown in Figure (d). Figure (e) shows the values for the failure stretch of the specimen and the corresponding histogram. Figure (f) shows the values for the fracture energy and the corresponding histogram.

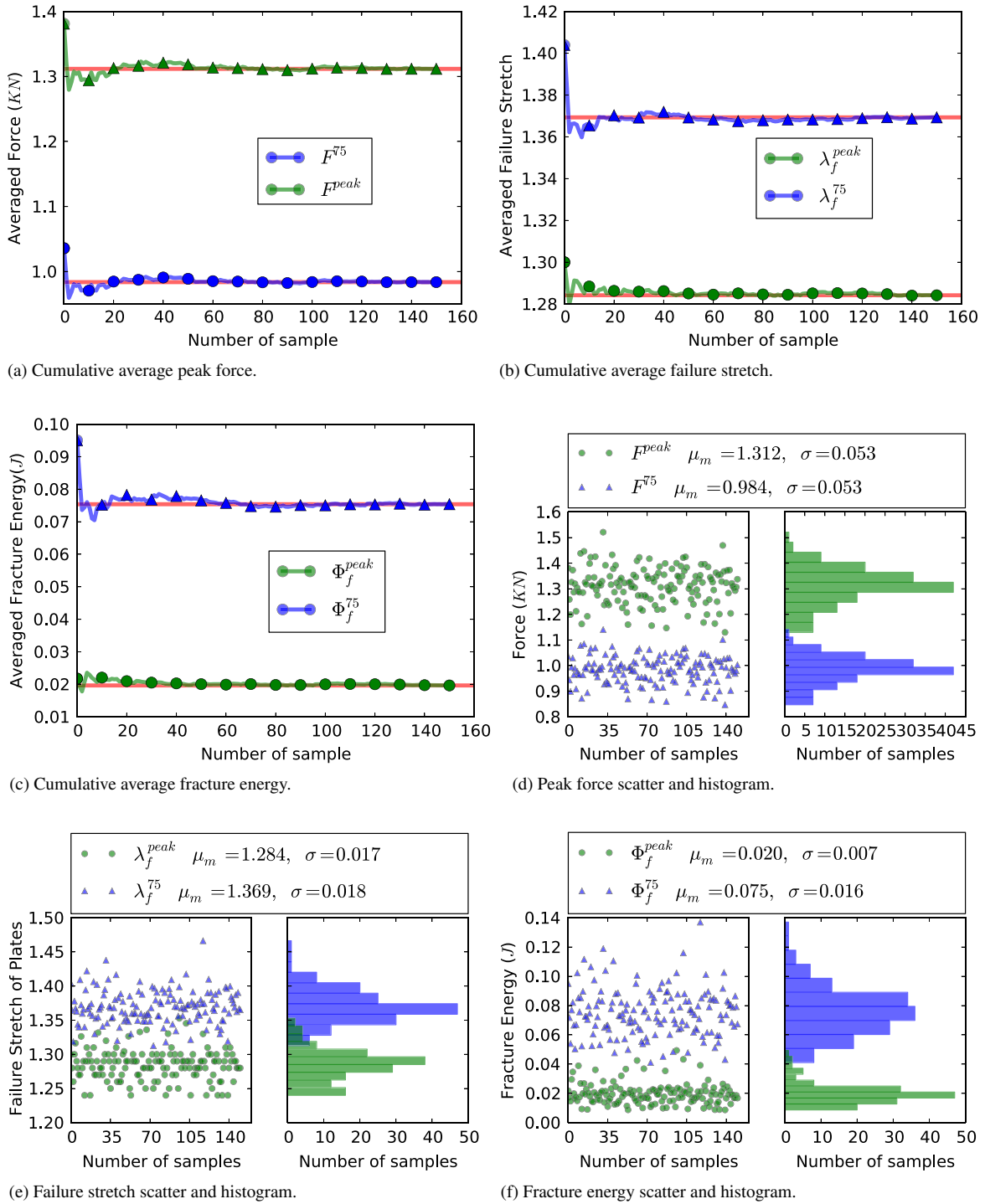
From Figs. 21–23(a) and (d), it can be seen that the values of F^{peak} and F^{75} have the same standard deviation, σ but different mean value, μ_m values. This is an expected result since F^{75} is computed directly from the peak value.

The difference between the distributions observed in Section 5.1 for λ_f^{peak} and λ_f^{75} , respectively, and for Φ_f^{peak} and Φ_f^{75} , respectively, are also observed in this subsection. For example, as seen in Fig. 21(e), the σ value of λ_f^{peak} is 0.005, while it is 0.011 for λ_f^{75} . The σ value of Φ_f^{peak} is 0.007, but increases to 0.034 at failure. Hence, similar as the realizations with voids, the uncertainty increases at failure.

The results from all three volume fractions are shown in Fig. 24, where the variations of the force, stretch and fracture energy are summarized. As can be seen in Figs. 24(a) and 24(b), while the peak force average and the failure force average increase dramatically, the peak stretch average and the failure stretch average drop (see Figs. 24(c) and 24(d)). Furthermore, as can be seen in Figs. 24(e) and 24(f), the peak fracture energy average drops slowly, while the failure fracture energy average increases at first but then drops.

5.3. Case 3: samples with high inclusion/matrix stiffness ratio

Finally, we consider the case that rubber is reinforced by very stiff carbon black particles. The parameters used for the rubber, very stiff CB particles and phase field are summarized in Table 1. The volume fractions of CB in this set also take the following values: 10%, 20% and 30%. The configurations adopted in the second set are used here. A representative sample with volume fraction 30% is shown in Fig. 18.

Fig. 14. Statistics from MC simulations of natural rubber with volume fraction $v = 10\%$ voids.

The results of the MC simulations are reported in Figs. 25–27 for different volume fractions of 10%, 20% and 30%. In all of these plots, Figure (a) shows the evaluation of the average cumulative peak force versus the current realization number. The evaluation of the average cumulative failure stretch and of the average cumulative fracture energy is given in (b) and (c), respectively.

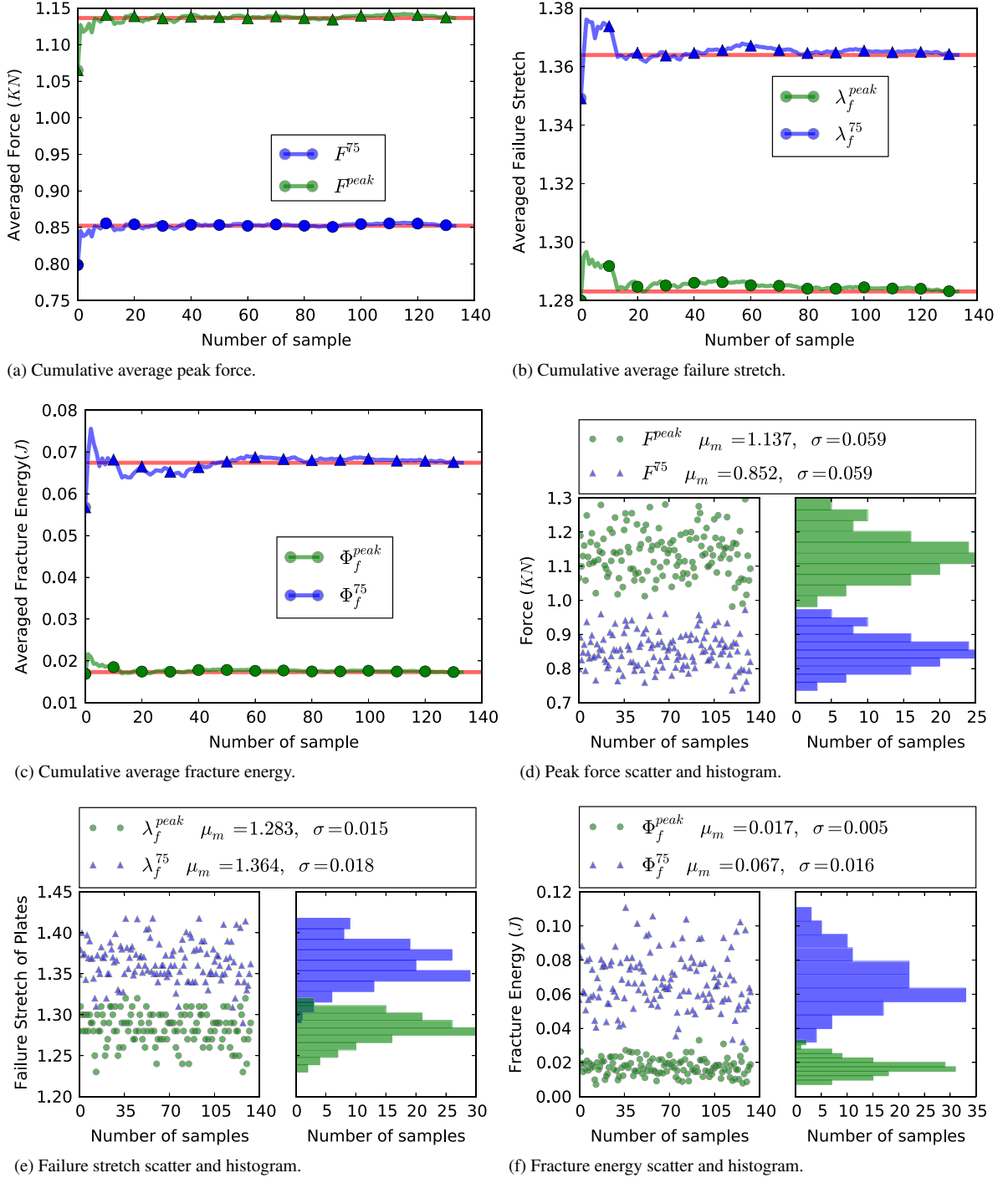
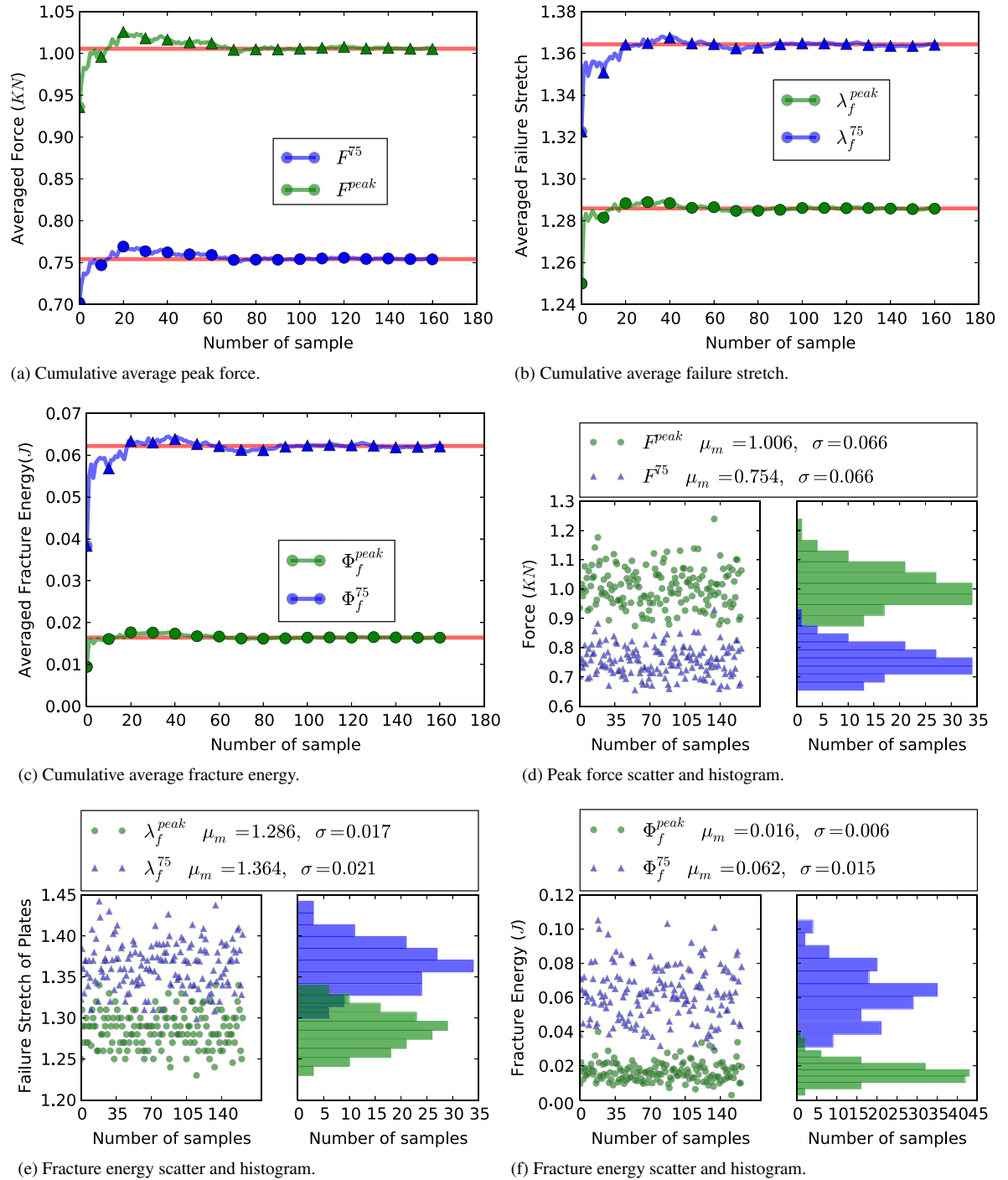


Fig. 15. Statistics from MC simulations of natural rubber with volume fraction $v = 15\%$ voids.

The peak force for every realization and its corresponding histogram is shown in Figure (d). Figure (e) shows the values for the failure stretch of the specimen and the corresponding histogram. Figure (f) shows the values for the fracture energy and the corresponding histogram.

From Figs. 25 to 27(a) and (d), it can be seen that the values of F^{peak} and F^{75} have the same standard deviation, σ but different mean value, μ_m values. This is an expected result since F^{75} is computed directly from the peak value.

Fig. 16. Statistics from MC simulations of natural rubber with volume fraction $v = 20\%$ voids.

The difference observed in Sections 5.1 and 5.2 between the distributions for λ_f^{peak} and λ_f^{75} , respectively, and for F_f^{peak} and Φ_f^{75} , respectively, are also observed in this subsection. For example, as seen in Fig. 25(e), the σ value of λ_f^{peak} is 0.005, while it is 0.011 for λ_f^{75} . The σ value of Φ_f^{peak} is 0.007, but increases to 0.036 at failure. Hence, similar as the realizations with voids, the uncertainty increases at failure.

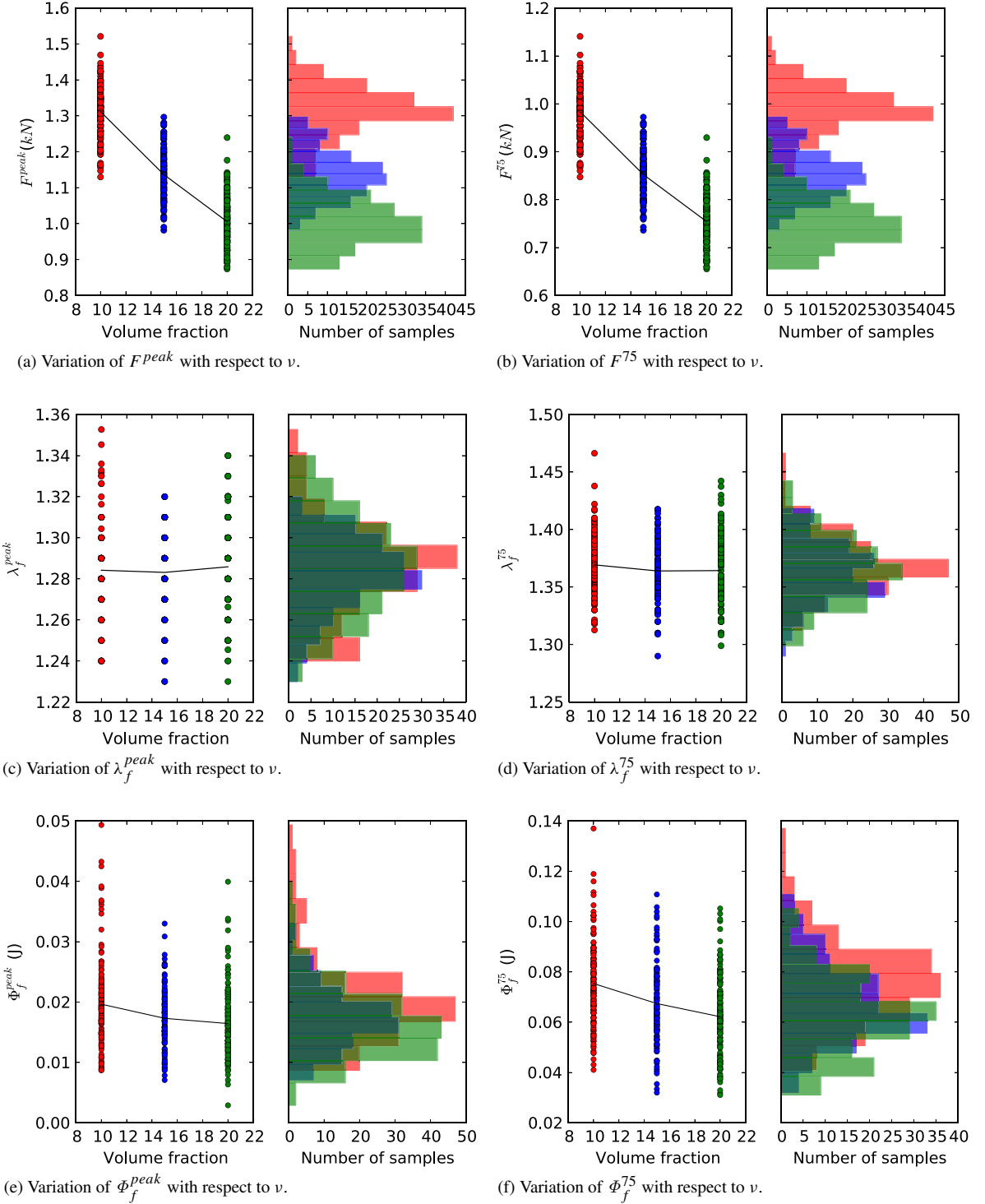


Fig. 17. Summary of the Statistics obtained in Figs. 14–16 in terms of force, stretch and fracture energy at peak and at failure points, as a function of the volume fraction of voids.

The results from all three volume fractions are shown in Fig. 28, where the variations of the force, stretch and fracture energy are summarized. As can be seen in Figs. 28(a) and 28(b), while the peak force average and the failure force average increase dramatically, the peak stretch average and the failure stretch average drop (see Figs. 28(c) and

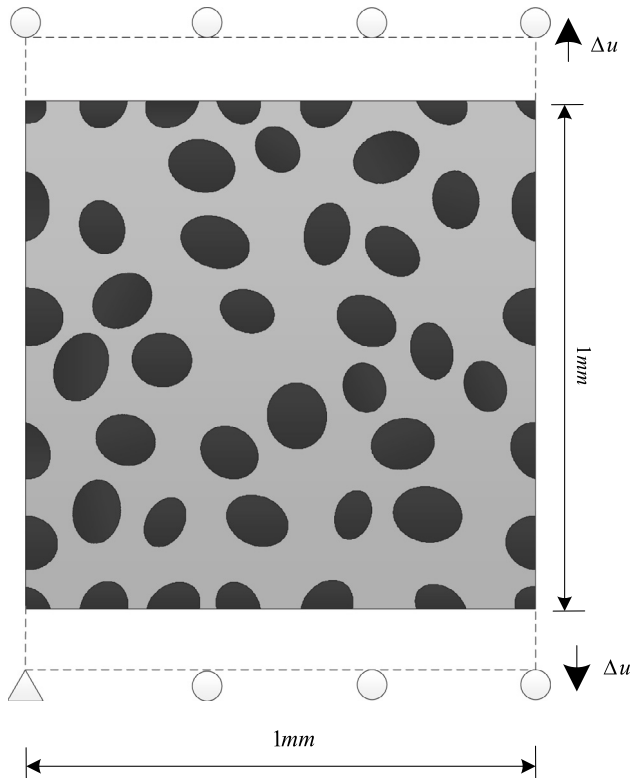


Fig. 18. Geometry and boundary conditions of carbon black reinforced natural rubber sample in one representative MC realization, volume fraction $\nu = 30\%$. Δu indicates a displacement control approach used to stretch the sample until its rupture.

28(d)). Furthermore, the trend shown in Section 5.2 can also be observed in Figs. 28(e) and 28(f). The peak fracture energy average drops slowly, while the failure fracture energy average increases at first but then drops.

5.4. Discussion

Comparing all of the aforementioned results for Natural Rubber with distributed elliptical voids or reinforced stiff/very stiff Carbon Black inclusions, the following conclusions can be drawn with respect to rupture behavior:

1. The increase of the volume fraction of CB increases the peak force of the material (see Figs. 24(a) and 28(a)), while the increase of the volume fraction of voids reduces the peak force as shown in Fig. 17(a). This is expected since the presence of voids weakens the composite material while the presence of stiffer inclusions strengthens it.
2. The difference between the results of stiff and very stiff inclusions is not significant when comparing Figs. 24 and 28. Even though the stiffness of CB particles increases by two orders of magnitude, it only has a limited effect on the strength of the composite. In other words, increasing the stiffness of the particles beyond a certain value can no longer continue to improve the effect of reinforcement in terms of failure mechanics since the cracks would still propagate through the weakest material which is the rubber.
3. Increasing volume fraction of CB particles significantly increases the peak and failure loads while at the same time reducing the fracture stretch of the composite rubber material, as can be seen in Figs. 24(c) and 28(c). This means that with the increase in volume fraction of CB, the composite material becomes more brittle.

On the other hand, increasing the volume fraction of voids has almost no effect on the fracture stretch of pure rubber (see Figs. 17(c) and 17(d)). In other words, a pure rubber material with voids essentially still deforms in the same fashion but has significantly less strength.

4. The reinforcement by CB particles cannot dramatically increase the composite material's fracture energy Φ_f^{75} , as noted in Figs. 24(f) and 28(f). Moreover, an excess of CB particles decreases the material fracture toughness by making the material more brittle. In this sense, a volume fraction of 20% is the best value in terms of material fracture energy. However, more studies need to be carried out to obtain an overall optimal value.

Table 3

Number of samples that sustained the design load of 3.9 KN for a given volume fraction of $\nu = 30\%$.

Material	Fully ruptured samples	Survived samples
Stiff CB reinforced NR	45	69
Very stiff CB reinforced NR	57	59
Pure NR	All failed	

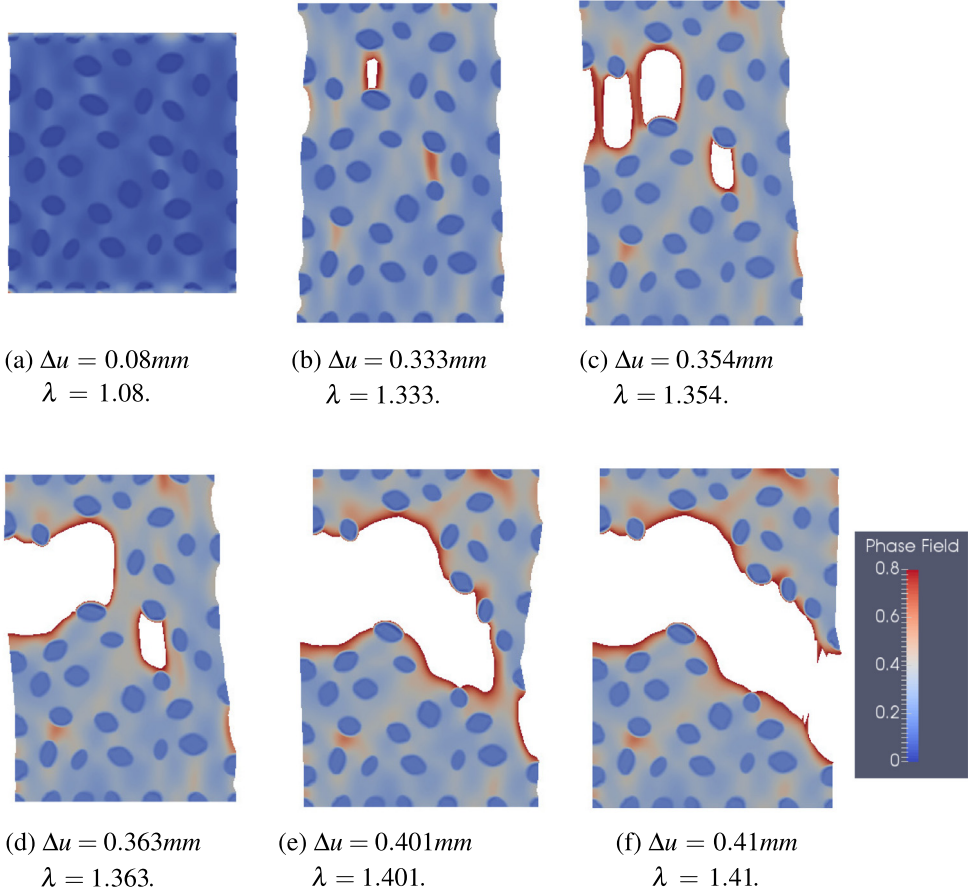


Fig. 19. Snapshots showing the complex crack propagation topology in the example realization in Fig. 18 due to large deformation stretching.

5. The uncertainty described by the variance, increases from peak stretch and peak fracture energy to their counterparts at failure, as can be seen in Figs. 14–16, 21–23, 25–27. This is also illustrated with scatter bars in Fig. 29. The scatter of fracture energy and stretch is significantly larger when failure occurs. Furthermore, comparing Figs. 14–16, 21–23 or 25–27, we note that for the NR with CB particles, the difference between the uncertainty of λ_f^{peak} and λ_f^{75} , and of Φ_f^{peak} and Φ_f^{75} is much larger than that of NR with voids.
6. The statistic analysis of failure presented in this paper has significant implications for the design of such composite materials. For example, consider an application where a composite material has to sustain a design load of 3.9 KN. To this end, consider the results for a case study with volume fraction $\nu = 30\%$ that are summarized in Table 3 where the number of samples that survived the load and those that failed and ruptured are given. This is also illustrated in Fig. 30 through force–displacement curves for pure rubber and stiff/very stiff CB reinforced NR for selected samples in each category.

These results reveal, to some extent, that failure uncertainty of CB reinforced NR with the same volume fraction and material parameters is an inherent property of this heterogeneous material. Hence, as opposed to homogenization

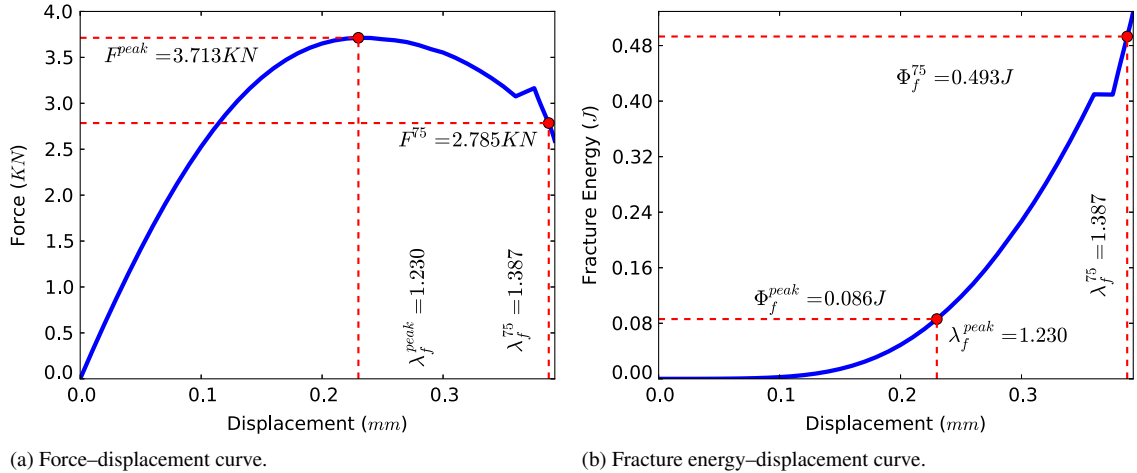


Fig. 20. Results from the example configuration in Figs. 18 and 19.

of material properties, statistic characterization of failure should be considered with great caution. For example if the design load in this example only slightly changes, the number of failed samples could significantly increase, which is to say that such failure mechanics problems may be very sensitive to small perturbations.

6. Conclusions

A Phase Field method for modeling the rupture of hyperelastic materials coupled with a Monte Carlo approach is proposed to quantify the uncertainty in the failure properties of Natural Rubber filled with voids or stiff/very stiff Carbon Black particles. The Phase Field method allows for modeling crack propagation without explicitly tracking crack surfaces which is especially useful for complex crack growth patterns in large deformations. The method is first validated with some available experimental data and then extended to Monte Carlo simulations of rubber with an arbitrary number, aspect ratio, location and orientation of embedded elliptical CB particles or voids. Quantities such as load, stretch and fracture energy corresponding to peak force and rupture (herein defined as when the force drops to 75% of its peak value) have been recorded to study the behavior of this composite material. While additional reinforcing particles enhance the fracture toughness of the composite, it becomes at the same time more brittle and the deformations it can sustain decrease. The main conclusion is that the uncertainty of the quantities monitored at failure is significantly larger than those corresponding to the peak state. Furthermore, we conclude that statistic quantification of failure mechanics processes, as opposed to homogenization of material properties, should be considered with great caution when designing such composite materials since the statistics can be very sensitive to the failure state. Thus, additional research in stochastic mechanics of failure analysis is required to characterize such problems with complex fracture patterns at large deformations.

Acknowledgments

This research was supported by the National Natural Science Foundation of China, NSFC (11472194); and the Ministry of Science and Technology of China (Grant No. SLDRC14-B-28). The first author would like to acknowledge the financial support from China Scholarship Council (CSC) (201406260089) for his two-year visit to Columbia University where this collaborative work was carried out.

Appendix

In this section, the specific expression of the Jacobian matrix in Eq. (37) was derived. The variation of the momentum equation with respect to displacement is computed as

$$J_i^{uu} \delta u_i = \delta R^{uu} [\delta u_i] = \lim_{\varepsilon \rightarrow 0} \frac{1}{\varepsilon} (R^u [u_i + \varepsilon \delta u_i] - R^u [u_i]) = \frac{d}{d\varepsilon} R^u [u_i + \varepsilon \delta u_i] \Big|_{\varepsilon=0}. \quad (48)$$

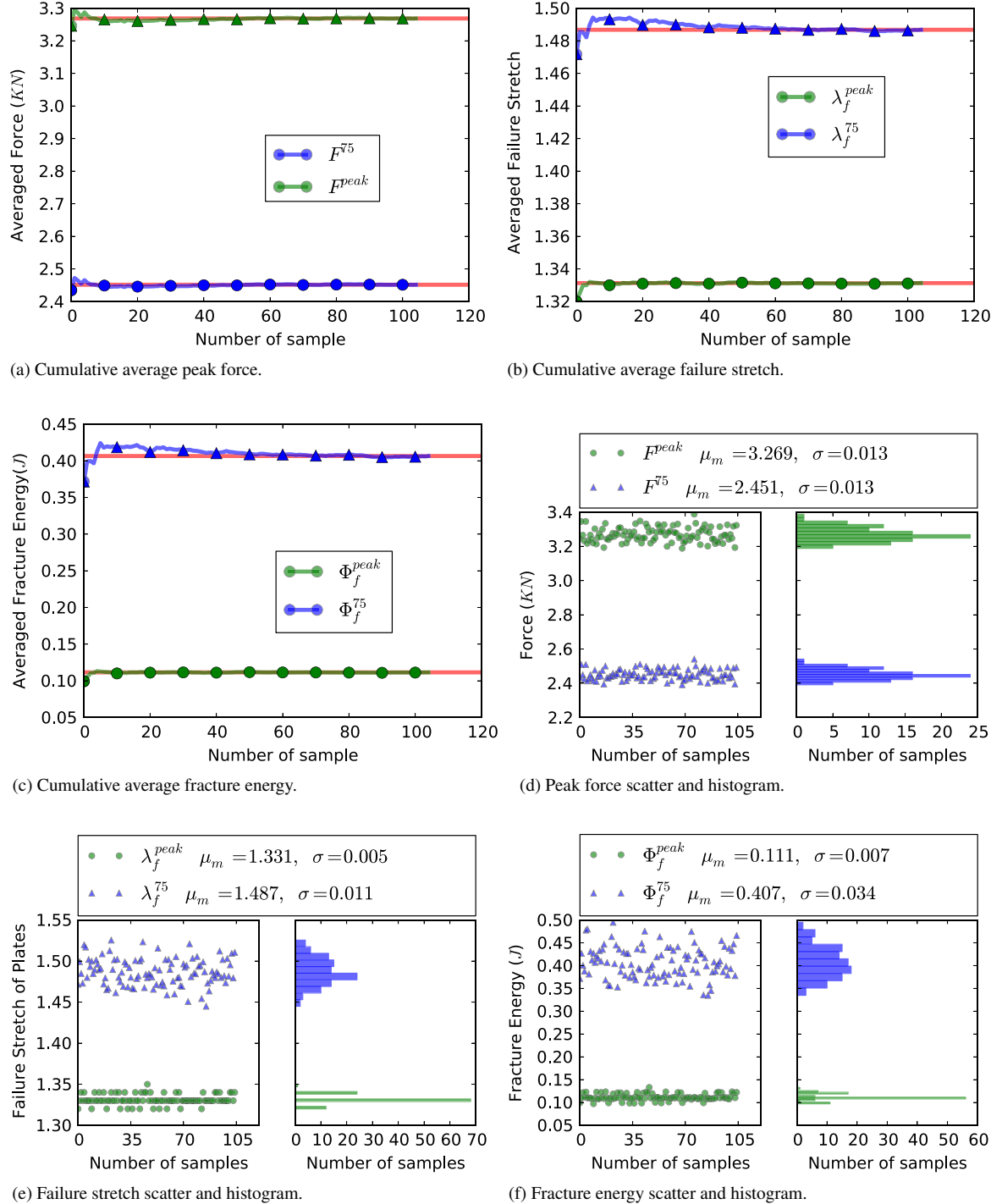
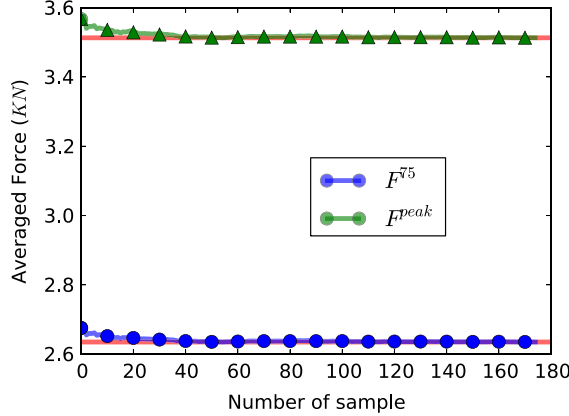


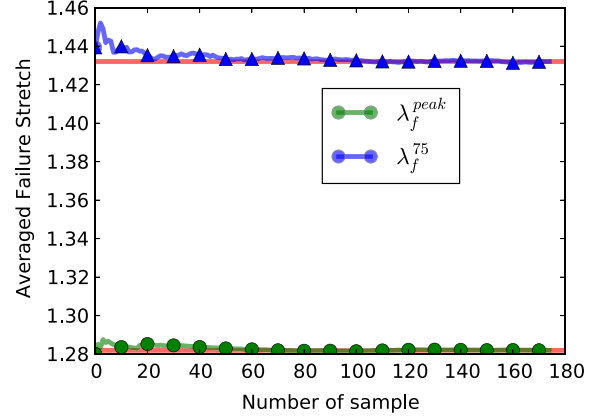
Fig. 21. Statistics from MC simulations of natural rubber reinforced by stiff carbon black particles with volume fraction $v = 10\%$.

Plugging (32) into (48) and separating the derivative into two parts due to the $F_{A_j}^{-1}$ term and the τ_{ij} term leads to

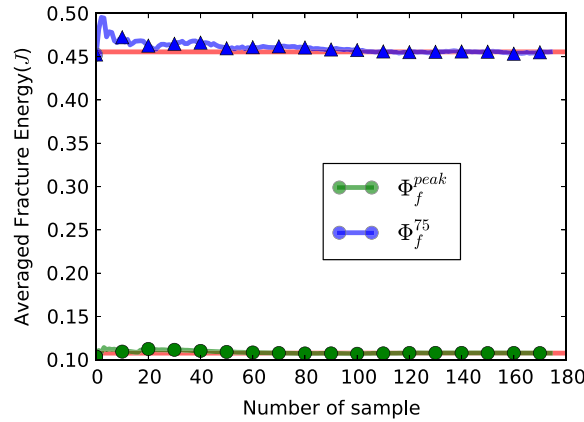
$$\delta R^{uu} = \delta R^{F_{A_j}^{-1}} + \delta R^{\tau_{ij}}, \quad (49)$$



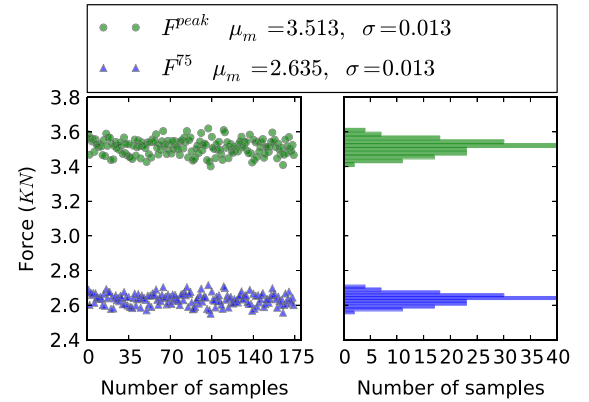
(a) Cumulative average peak force.



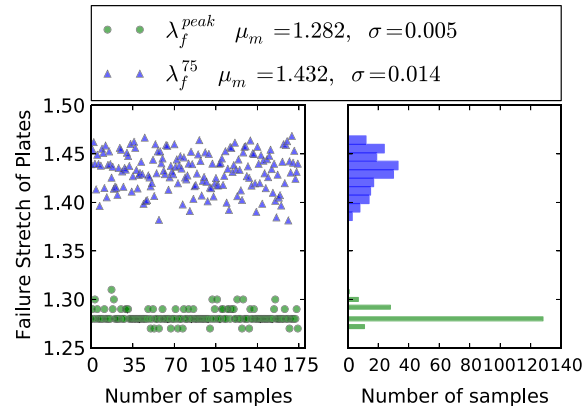
(b) Cumulative average failure stretch.



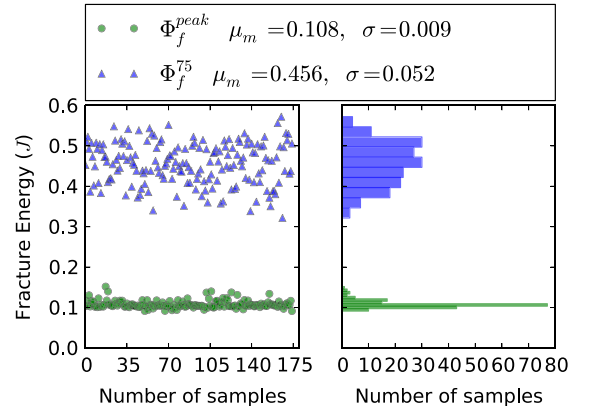
(c) Cumulative average fracture energy.



(d) Peak force scatter and histogram.



(e) Failure stretch scatter and histogram.



(f) Fracture energy scatter and histogram.

Fig. 22. Statistics from MC simulations of natural rubber reinforced by stiff carbon black particles with volume fraction $\nu = 20\%$ weak carbon black.

where

$$\delta R^{F_{Aj}^{-1}} = \int_{\Omega_0} w_{i,A}^u \left(\delta F_{Aj}^{-1} [\delta u_j] \right) \tau_{ij} d\Omega_0. \quad (50)$$

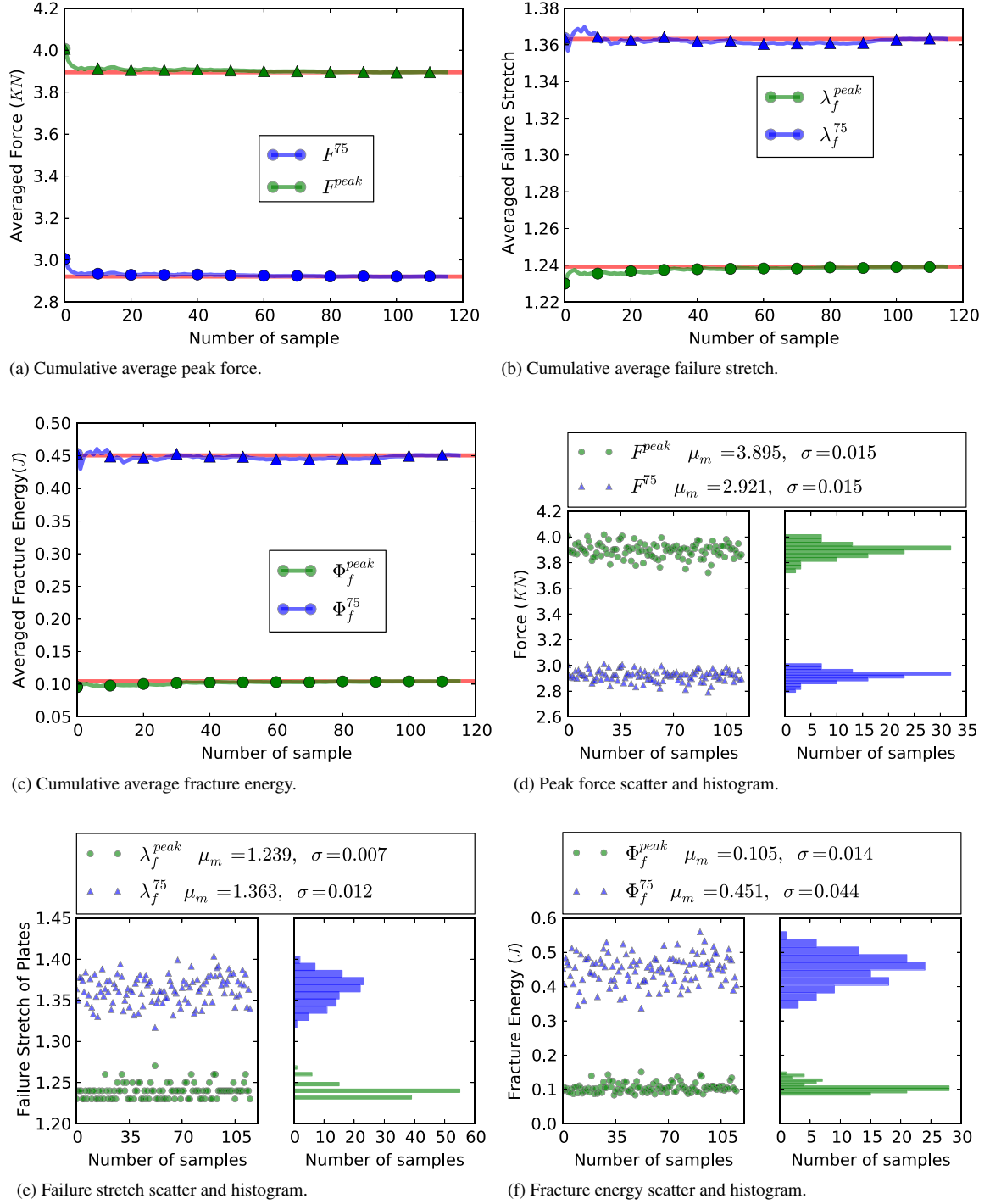


Fig. 23. Statistics from MC simulations of natural rubber reinforced by stiff carbon black particles with volume fraction $\nu = 30\%$ weak carbon black.

According to the equation in [62]

$$\lim_{\varepsilon \rightarrow 0} \frac{1}{\varepsilon} \left(F_{A_j}^{-1} [u_j + \varepsilon \delta u_j] - F_{A_j}^{-1} [u_j] \right) = -F_{A_k}^{-1} \delta u_{k,j}, \quad (51)$$

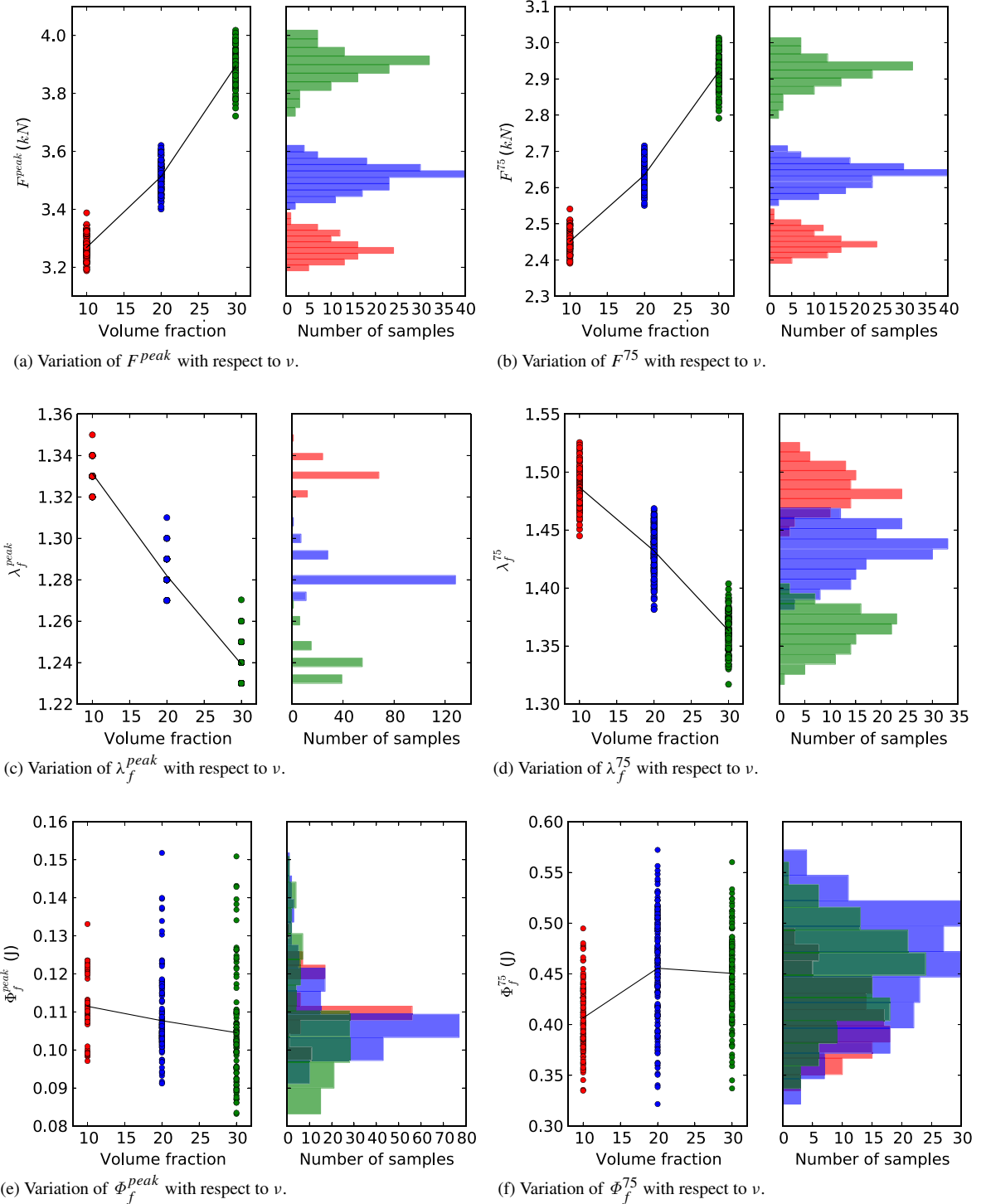
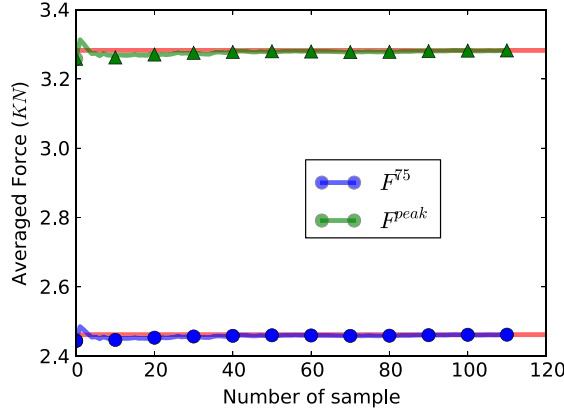


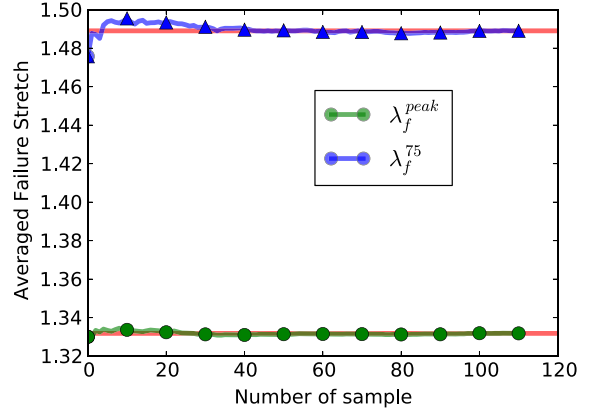
Fig. 24. Summary of the Statistics obtained in Figs. 21–23 in terms of force, stretch and fracture energy at peak and at failure points, as a function of increased volume fraction of carbon black.

Eq. (50) could be rewritten as

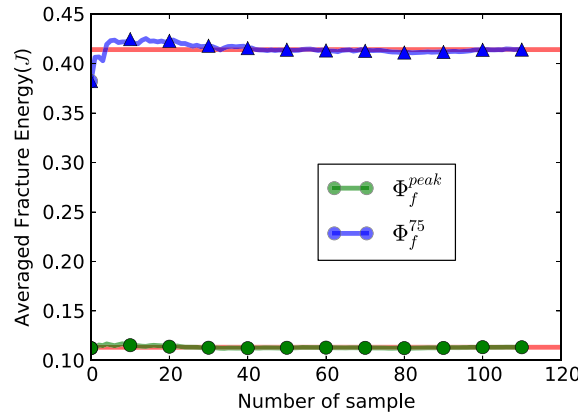
$$\delta R^{F_{A,j}^{-1}} = - \int_{\Omega_0} w_{i,A}^u F_{Ak}^{-1} \delta u_{k,j} \tau_{ij} d\Omega_0. \quad (52)$$



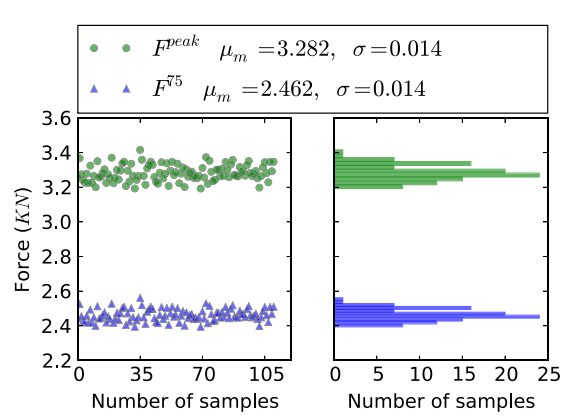
(a) Cumulative average peak force.



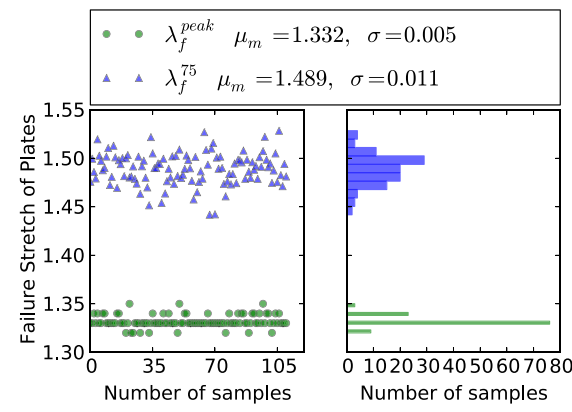
(b) Cumulative average failure stretch.



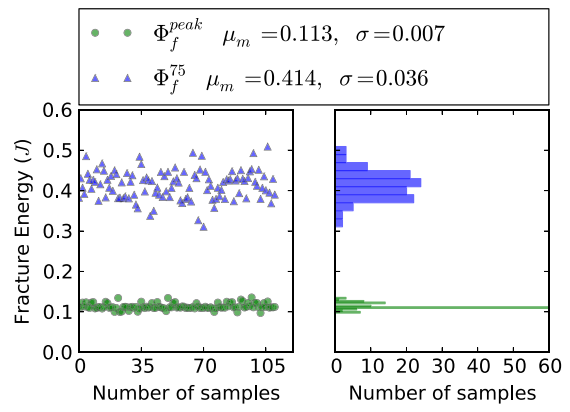
(c) Cumulative average fracture energy.



(d) Peak force scatter and histogram.



(e) Failure stretch scatter and histogram.

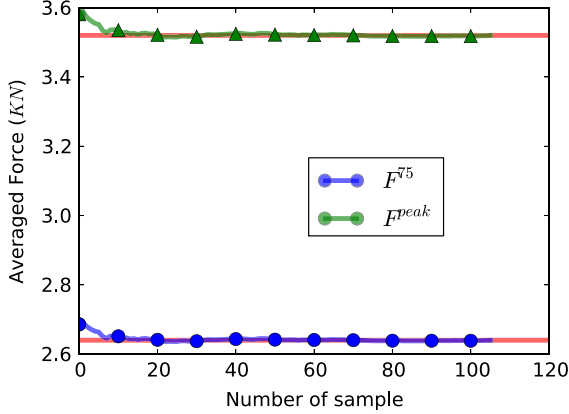


(f) Fracture energy scatter and histogram.

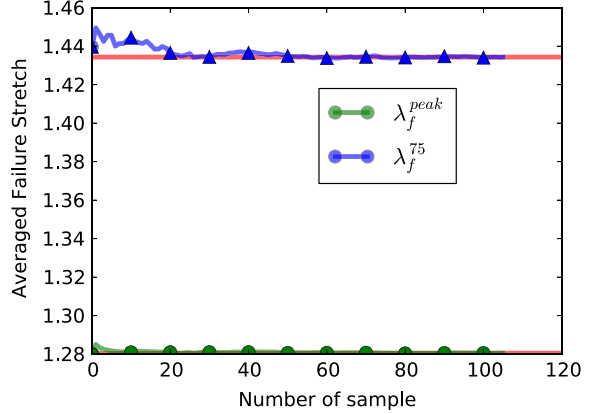
Fig. 25. Statistics from MC simulations of natural rubber reinforced by very stiff carbon black particles with volume fraction $\nu = 10\%$ stiff carbon black.

Also we have

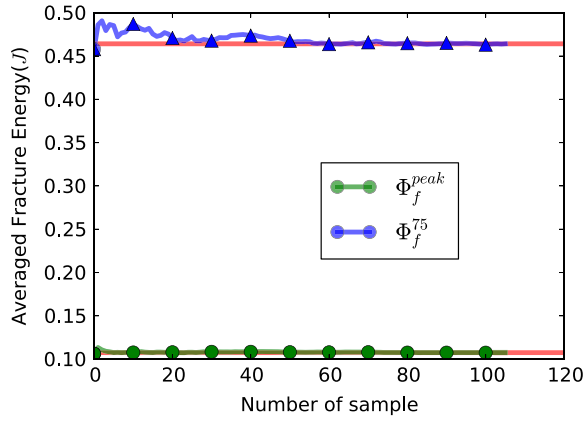
$$\delta R^{\tau_{ij}} = \int_{\Omega_0} w_{i,A}^u F_{A,j}^{-1} (\delta \tau_{ij} [\delta u_j]) d\Omega_0. \quad (53)$$



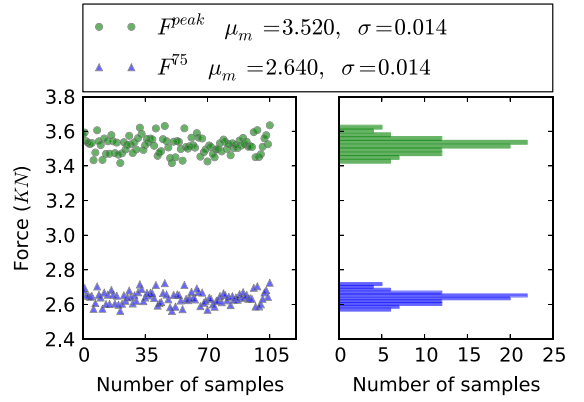
(a) Cumulative average peak force.



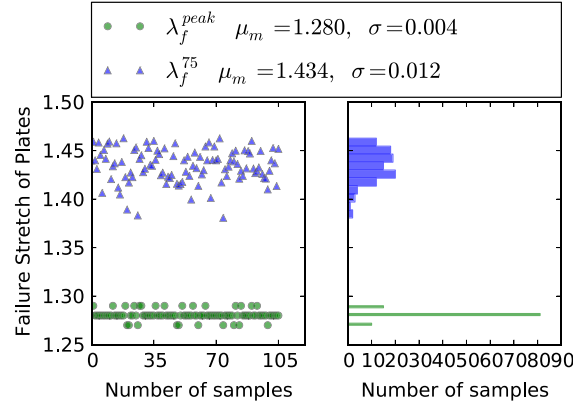
(b) Cumulative average failure stretch.



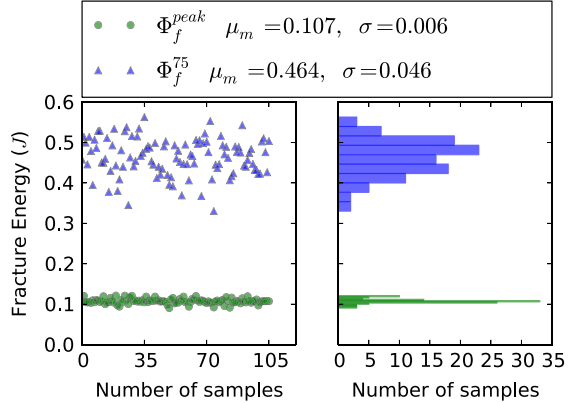
(c) Cumulative average fracture energy.



(d) Peak force scatter and histogram.



(e) Failure stretch scatter and histogram.



(f) Fracture energy scatter and histogram.

Fig. 26. Statistics from MC simulations of natural rubber reinforced by very stiff carbon black particles with volume fraction $\nu = 20\%$ stiff carbon black.

Based on the Arruda–Boyce model and the phase field degrade function introduced from Eq. (20) to (24), the $\delta\tau_{ij}[\delta u_j]$ could be separated into three parts due to the $\text{dev}(b_{ij})$ term, the $\text{tr}(b_{ij})$ term and the J term, which could be expressed as,

$$\delta\tau_{ij}[\delta u_j] = \delta\tau_{ij}^{\text{dev}(b_{ij})}[\delta u_j] + \delta\tau_{ij}^{\text{tr}(b_{ij})}[\delta u_j] + \delta\tau_{ij}^J[\delta u_j]. \quad (54)$$

Here,

$$\delta\tau_{ij}^{\text{tr}(b_{ij})}[\delta u_j] = m(c)C_1(4\alpha_2 + 12\alpha_3\bar{b}_{kk} + 24\alpha_4\bar{b}_{kk}^2 + 40\alpha_5\bar{b}_{kk}^3)\text{dev}(\bar{b}_{ij})\frac{d\bar{b}_{kk}}{du_j}\delta u_j, \quad (55)$$

$$\delta\tau_{ij}^{\text{dev}(b_{ij})}[\delta u_j] = m(c)C_1(2\alpha_1 + 4\alpha_2\bar{b}_{kk} + 6\alpha_3\bar{b}_{kk}^2 + 8\alpha_4\bar{b}_{kk}^3 + 10\alpha_5\bar{b}_{kk}^4)\frac{d(\text{dev}(\bar{b}_{ij}))}{du_j}\delta u_j, \quad (56)$$

$$\delta\tau_{ij}^J[\delta u_j] = \begin{cases} m(c)\frac{K_m}{J}\frac{dJ}{du_j}\delta u_j & J \geq 1 \\ \frac{K_m}{J}\frac{dJ}{du_j}\delta u_j & J < 1. \end{cases} \quad (57)$$

As introduced in [62], the linearization of the J , and b_{ij} could be written as

$$\lim_{\varepsilon \rightarrow 0} \frac{1}{\varepsilon} \left(J[u_j + \varepsilon\delta u_j] - J[u_j] \right) = J\delta u_{k,k}, \quad (58)$$

$$\lim_{\varepsilon \rightarrow 0} \frac{1}{\varepsilon} \left(b_{ij}[u_j + \varepsilon\delta u_j] - b_{ij}[u_j] \right) = \delta u_{i,l}b_{lj} + b_{il}\delta u_{j,l}. \quad (59)$$

With above equations at hand, the variation $\frac{d\bar{b}_{kk}}{du_j}\delta u_j$ could be expressed as

$$\frac{d\bar{b}_{kk}}{du_j}\delta u_j = -\frac{2}{3}J^{-\frac{5}{3}}J\delta u_{k,k}b_{kk} + J^{-\frac{2}{3}}\left(\delta u_{k,l}b_{lk} + b_{kl}\delta u_{k,l}\right), \quad (60)$$

while the variation $\frac{d(\text{dev}\bar{b}_{ij})}{du_j}\delta u_j$ could be expressed as

$$\frac{d(\text{dev}\bar{b}_{ij})}{du_j}\delta u_j = -\frac{2}{3}J^{-\frac{5}{3}}J\delta u_{k,k}\text{dev}b_{ij} + J^{-\frac{2}{3}}\left(\frac{d(b_{ij} - \frac{1}{3}b_{kk}\delta_{ij})}{du_j}\right). \quad (61)$$

After some index manipulation, R^{uu} is

$$\delta R^{uu} = \int_{\Omega_0} w_{i,A}^u \left(-F_{Aj}^{-1}\tau_{il}\delta_{jk} + F_{Aj}^{-1}(\delta\tau_{ik}[\delta u_j])\delta_{lj} \right) \delta u_{k,l} d\Omega_0. \quad (62)$$

With equations from (49), and substituting the Galerkin approximation shown in (34), the spatial discretized equation of R^{uu} could be written as

$$\delta \mathbf{R}_\alpha^{uu} = \mathbf{J}_{\alpha\beta}^{uu} \delta \hat{u}_\beta = \int_{\Omega_0} N_{i\alpha,A}^u \left(-F_{Aj}^{-1}\tau_{il}\delta_{jk} + F_{Aj}^{-1}(\delta\tau_{ik}[\delta u_j])\delta_{lj} \right) N_{k\beta,B}^u F_{Bl}^{-1} d\Omega_0 \delta \hat{u}_\beta, \quad (63)$$

or

$$\mathbf{J}_{\alpha\beta}^{uu} = \int_{\Omega_0} N_{i\alpha,A}^u \left(-F_{Aj}^{-1}\tau_{il}\delta_{jk} + F_{Aj}^{-1}(\delta\tau_{ik}[\delta u_j])\delta_{lj} \right) N_{k\beta,B}^u F_{Bl}^{-1} d\Omega_0. \quad (64)$$

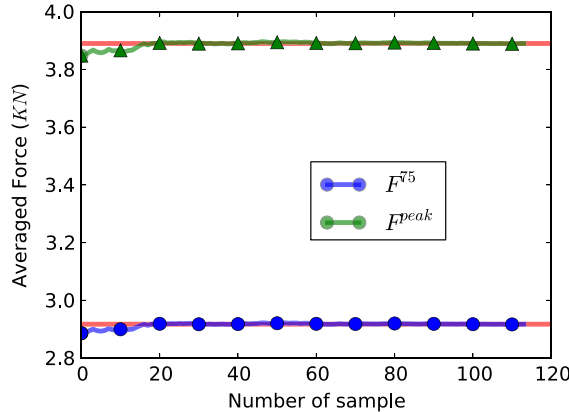
The first term arises from geometric nonlinearity while the second term raises from material nonlinearity, and are denoted as $\mathbf{L}_{\alpha\beta}^{uu}$ and $\mathbf{G}_{\alpha\beta}^{uu}$, respectively.

The variation of the momentum equation with respect to phase field is computed as

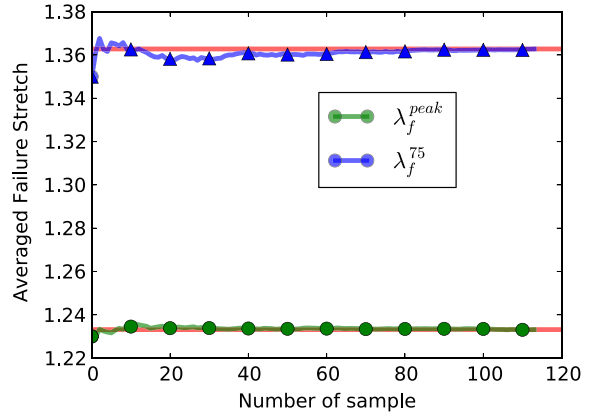
$$J_i^{uc}\delta c = \delta R^{uc}[\delta c] = \lim_{\varepsilon \rightarrow 0} \frac{1}{\varepsilon} \left(R^u[c + \varepsilon\delta c] - R^u[c] \right) = \frac{d}{d\varepsilon} R^u[c + \varepsilon\delta c] \Big|_{\varepsilon=0}. \quad (65)$$

Plugging (32) into (65) gives

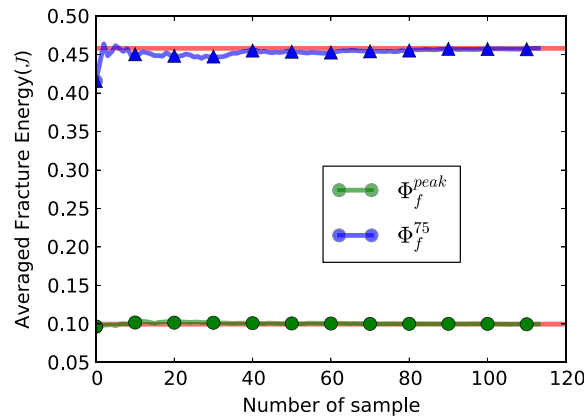
$$\delta R^{uc} = \int_{\Omega_0} w_{i,A}^u F_{Aj}^{-1}(\delta\tau_{ij}[\delta c]) d\Omega_0. \quad (66)$$



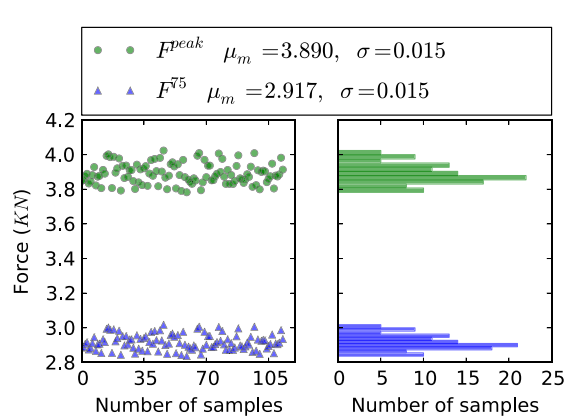
(a) Cumulative average peak force.



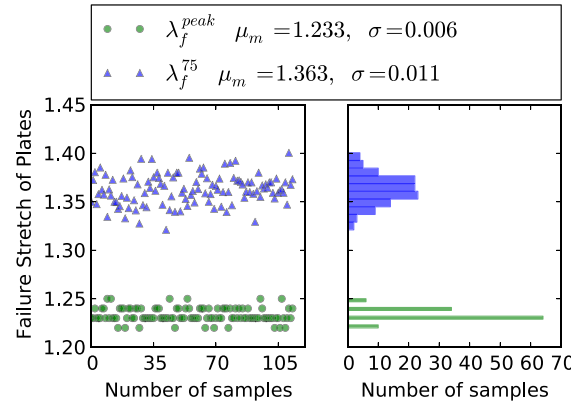
(b) Cumulative average failure stretch.



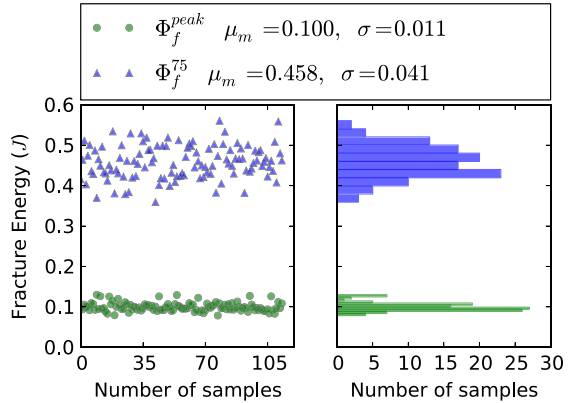
(c) Cumulative average fracture energy.



(d) Peak force scatter and histogram.



(e) Failure stretch scatter and histogram.



(f) Fracture energy scatter and histogram.

Fig. 27. Statistics from MC simulations of natural rubber reinforced by very stiff carbon black particles with volume fraction $\nu = 30\%$ stiff carbon black.

Based on the Arruda–Boyce model and the phase field degrade function introduced from Eq. (20) to (24), if $J \geq 1$,

$$\delta \tau_{ij}[\delta c] = \frac{\partial m(c)}{\partial c} \left(C_1 (2\alpha_1 + 4\alpha_2 \bar{b}_{kk} + 6\alpha_3 \bar{b}_{kk}^2 + 8\alpha_4 \bar{b}_{kk}^3 + 10\alpha_5 \bar{b}_{kk}^4) \text{dev}(\bar{b}_{ij}) + K_m \ln J \delta_{ij} \right) \delta c. \quad (67)$$

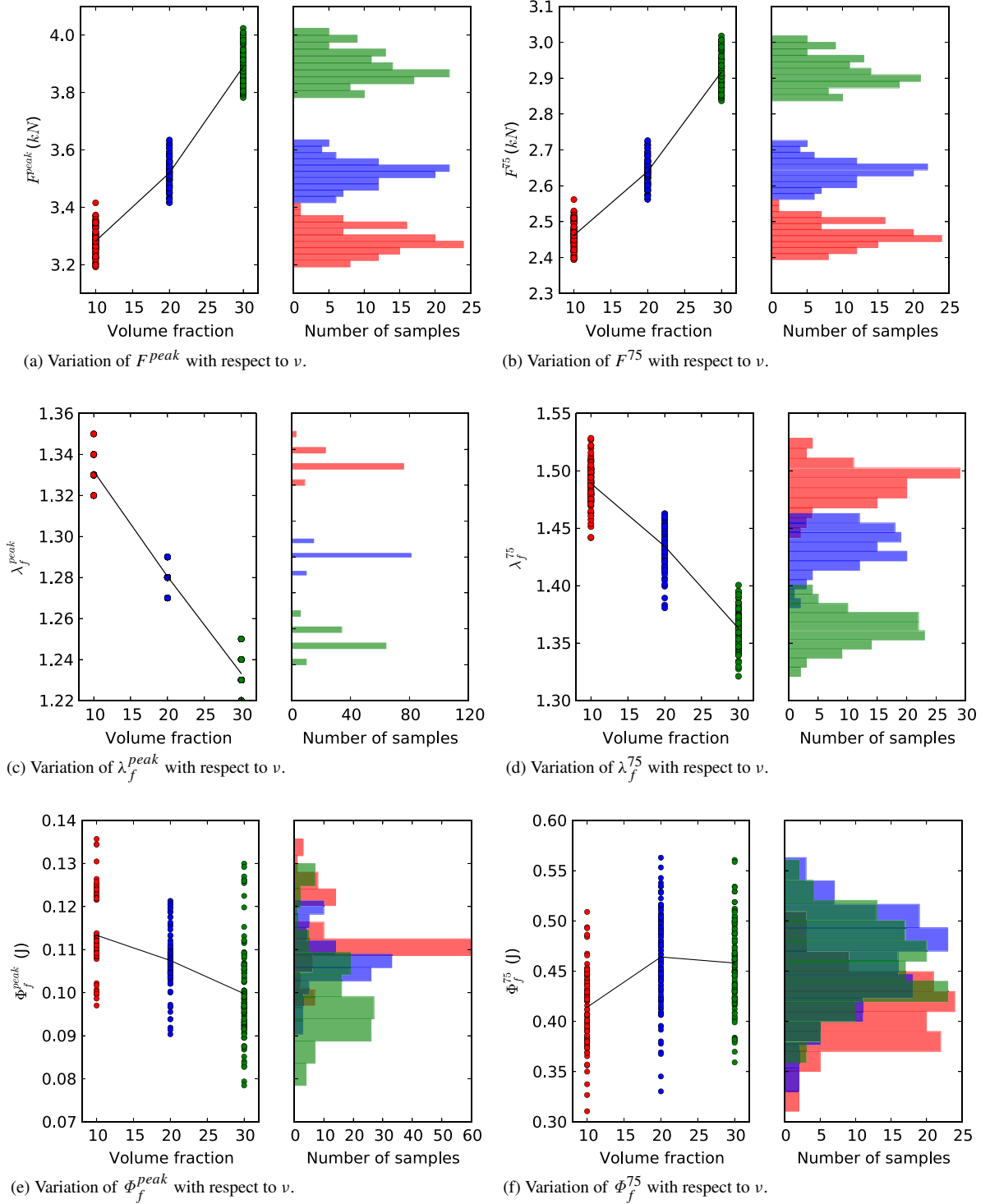


Fig. 28. Summary of the Statistics obtained in Figs. 25–27 in terms of force, stretch and fracture energy at peak and at failure points, as a function of increased volume fraction of Carbon Black.

If $J < 1$,

$$\delta\tau_{ij}[\delta c] = \frac{\partial m(c)}{\partial c} C_1 (2\alpha_1 + 4\alpha_2 \bar{b}_{kk} + 6\alpha_3 \bar{b}_{kk}^2 + 8\alpha_4 \bar{b}_{kk}^3 + 10\alpha_5 \bar{b}_{kk}^4) \text{dev}(\bar{b}_{ij}) \delta c. \quad (68)$$

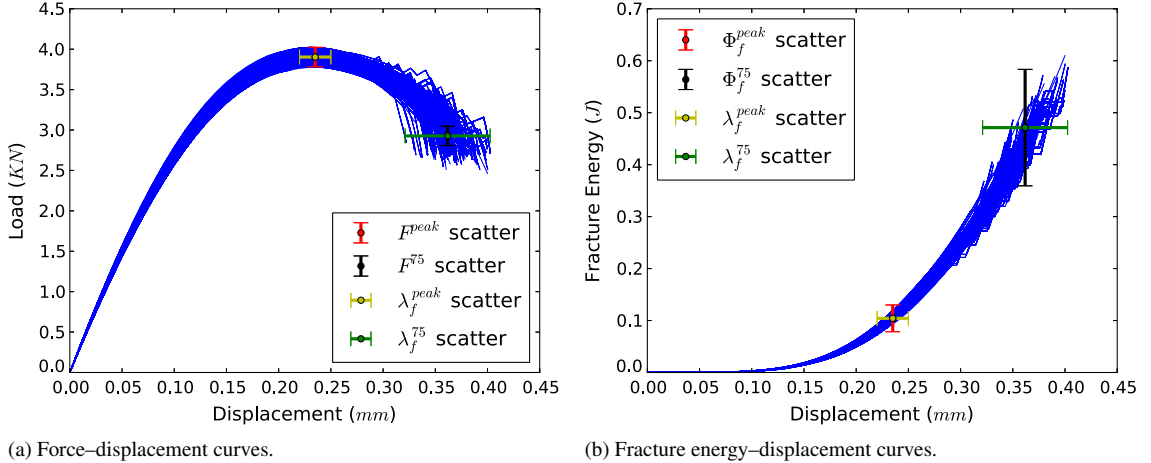


Fig. 29. Curves corresponding to the response of very stiff CB reinforced NR (volume fraction $v = 30\%$) obtained from all MC realizations. Error bars indicate scatter results at peak and at failure. Note that the uncertainty in fracture energy and stretch increases at the point of failure.

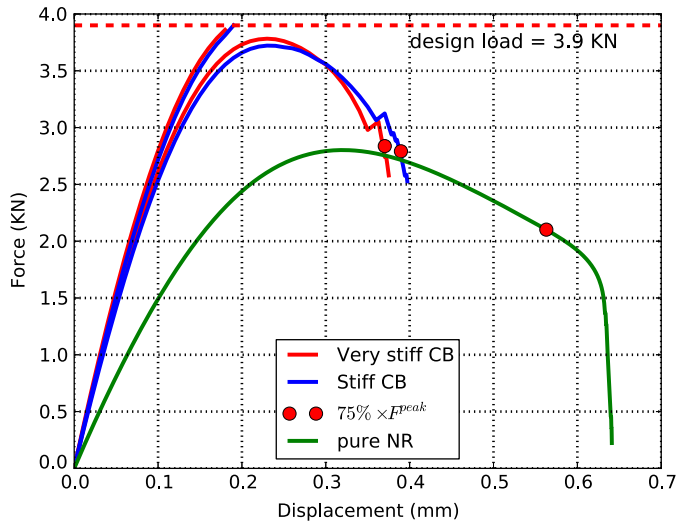


Fig. 30. The design load and the force–displacement curves of pure natural rubber and rubber reinforced by stiff/very stiff CB. Some samples were able to sustain the design load while others failed.

Substituting the Galerkin approximation shown in (34), the spatial discretized equation of R^{uc} could be written as

$$\delta \mathbf{R}_\alpha^{uc} = \mathbf{J}_{\alpha\kappa}^{uc} \delta \hat{c}_\kappa = \int_{\Omega_0} N_{i\alpha,A}^u F_{Aj}^{-1} (\delta \tau_{ij} [\delta c]) N_\kappa^c d\Omega_0 \delta \hat{c}_\kappa, \quad (69)$$

or

$$\mathbf{J}_{\alpha\kappa}^{uc} = \int_{\Omega_0} N_{i\alpha,A}^u F_{Aj}^{-1} (\delta \tau_{ij} [\delta c]) N_\kappa^c d\Omega_0. \quad (70)$$

This term arises from the derivative of degradation function $m(c)$ with respect to phase field and is denoted as $\mathbf{C}_{\alpha\kappa}^{uc}$.

The variation of the micro force balance equation with respect to displacement is computed as

$$J^{cu} \delta u_i = \delta R^{cu} [\delta u_i] = \lim_{\varepsilon \rightarrow 0} \frac{1}{\varepsilon} (R^c [u_i + \varepsilon \delta u_i] - R^c [u_i]) = \frac{d}{d\varepsilon} R^c [u_i + \varepsilon \delta u_i] \Big|_{\varepsilon=0}. \quad (71)$$

Plugging (33) into (71) gives

$$\delta R^{cu} = \int_{\Omega_0} w^c \frac{2l_0}{G_c} \frac{\partial m}{\partial c} \delta W_0^+[\delta u_i] d\Omega_0. \quad (72)$$

Based on the equation from (15) to (18)

$$\delta W_0^+[\delta u_i] = \begin{cases} \delta \bar{W}[\delta \bar{b}_{kk}] \delta \bar{b}_{kk}[\delta u_j] & J < 1 \\ \delta \bar{W}[\delta \bar{b}_{kk}] \delta \bar{b}_{kk}[\delta u_j] + \delta U[\delta J] \delta J[\delta u_j] & J \geq 1. \end{cases} \quad (73)$$

The specific form of Eq. (73) could be deviated by substituting (16) into $\delta \bar{W}[\delta \bar{b}_{kk}]$

$$\delta \bar{W}[\delta \bar{b}_{kk}] = C_1(\alpha_1 + 2\alpha_2 \bar{b}_{kk} + 3\alpha_3 \bar{b}_{kk}^2 + 4\alpha_4 \bar{b}_{kk}^3 + 5\alpha_5 \bar{b}_{kk}^4), \quad (74)$$

and substituting (15) into $\delta U[\delta J]$

$$\delta U[\delta J] = \frac{K_m}{J}. \quad (75)$$

The specific form of $\delta \bar{b}_{kk}[\delta u_j]$ and $\delta J[\delta u_j]$ could be get from Eqs. (60) and (58), respectively. With above derivation, substituting the Galerkin approximation shown in (34), the spatial discretized equation of R^{cu} could be written as

$$\delta \mathbf{R}_{\psi\beta}^{cu} = \mathbf{J}_{\psi\beta}^{cu} \delta \hat{u}_\beta = \int_{\Omega_0} N_\psi^c \frac{2l_0}{G_c} \frac{\partial m}{\partial c} \delta W_0^+[\delta u_i] N_{i\beta,A}^u d\Omega_0 \delta \hat{u}_\beta, \quad (76)$$

or

$$\mathbf{J}_{\psi\beta}^{cu} = \int_{\Omega_0} N_\psi^c \frac{2l_0}{G_c} \frac{\partial m}{\partial c} \delta W_0^+[\delta u_i] N_{i\beta,A}^u d\Omega_0. \quad (77)$$

This term arises from the linearization of W^+ with respect to displacement and is denoted as $\mathbf{W}_{\psi\beta}^{cu}$.

The variation of the micro force balance equation with respect to phase field is computed as

$$J^{cc} \delta c = \delta R^{cc}[\delta c] = \lim_{\varepsilon \rightarrow 0} \frac{1}{\varepsilon} (R^c[c + \varepsilon \delta c] - R^c[c]) = \frac{d}{d\varepsilon} R^c[c + \varepsilon \delta c] \Big|_{\varepsilon=0}. \quad (78)$$

Plugging (33) into (78) gives

$$\delta R^{cc} = \int_{\Omega_0} \left(w^c \left(1 + \frac{2l_0}{G_c} \frac{\partial^2 m}{\partial c^2} W_0^+ \right) + 4l_0^2 w_{,A}^c \frac{dc,A}{dc} \right) d\Omega_0 \delta c = J^{cc} \delta c. \quad (79)$$

With above derivation, substituting the Galerkin approximation shown in (34), the spatial discretized equation of R^{cu} could be written as

$$\delta \mathbf{R}_{\psi\kappa}^{cc} = \mathbf{J}_{\psi\kappa}^{cc} \delta \hat{c}_\kappa = \int_{\Omega_0} N_\psi^c \left(1 + \frac{2l_0}{G_c} \frac{\partial^2 m}{\partial c^2} W_0^+ \right) N_\kappa^c d\Omega_0 \delta \hat{c}_\kappa + \int_{\Omega_0} N_{\psi,A}^c 4l_0^2 N_{\kappa,A}^c d\Omega_0 \delta \hat{c}_\kappa, \quad (80)$$

or

$$\mathbf{J}_{\psi\kappa}^{cc} = \int_{\Omega_0} N_\psi^c \left(1 + \frac{2l_0}{G_c} \frac{\partial^2 m}{\partial c^2} W_0^+ \right) N_\kappa^c d\Omega_0 + \int_{\Omega_0} N_{\psi,A}^c 4l_0^2 N_{\kappa,A}^c d\Omega_0. \quad (81)$$

The first term is the mass matrix and arises from the degradation function. The second term is the stiffness matrix and raises from Laplacian term in the strong form. These two terms are denoted as $\mathbf{M}_{\psi\kappa}^c$ and $\mathbf{K}_{\psi\kappa}^c$, respectively.

References

- [1] T. Sajjayanukul, P. Saeoui, C. Sirisinha, Experimental analysis of viscoelastic properties in carbon black-filled natural rubber compounds, *J. Appl. Polym. Sci.* 97 (6) (2005) 2197–2203.
- [2] P. Teh, Z. Mohd Ishak, A. Hashim, J. Karger-Kocsis, U. Ishiaku, On the potential of organoclay with respect to conventional fillers (carbon black, silica) for epoxidized natural rubber compatibilized natural rubber vulcanizates, *Journal of applied polymer science* 94 (6) (2004) 2438–2445.

- [3] J.-B. Le Cam, B. Huneau, E. Verron, L. Gornet, Mechanism of fatigue crack growth in carbon black filled natural rubber, *Macromolecules* 37 (13) (2004) 5011–5017.
- [4] S. Bazhenov, J. Li, A. Hiltner, E. Baer, Ductility of filled polymers, *Journal of applied polymer science* 52 (2) (1994) 243–254.
- [5] E. Herve, A. Zaoui, N-layered inclusion-based micromechanical modelling, *Internat. J. Engrg. Sci.* 31 (1) (1993) 1–10.
- [6] B. Omnes, S. Thuillier, P. Pilvin, Y. Grohens, S. Gillet, Effective properties of carbon black filled natural rubber: experiments and modeling, *Composites A* 39 (7) (2008) 1141–1149.
- [7] A. Bensoussan, J.-L. Lions, G. Papanicolaou, *Asymptotic Analysis For Periodic Structures*, Vol. 374, American Mathematical Soc., 2011.
- [8] E. Sánchez-Palencia, *Non-Homogeneous Media and Vibration Theory*, Vol. 127, Springer-Verlag, Berlin, 1980.
- [9] S. Ghosh, K. Lee, S. Moorthy, Multiple scale analysis of heterogeneous elastic structures using homogenization theory and voronoi cell finite element method, *Int. J. Solids Struct.* 32 (1) (1995) 27–62.
- [10] J. Guedes, N. Kikuchi, Preprocessing and postprocessing for materials based on the homogenization method with adaptive finite element methods, *Comput. Methods Appl. Mech. Engrg.* 83 (2) (1990) 143–198.
- [11] K. Terada, N. Kikuchi, Nonlinear homogenization method for practical applications, *Appl. Mech. Div. Publ.* 212 (1995) 1–16.
- [12] J. Fish, V. Belsky, Multi-grid method for periodic heterogeneous media part 2: Multiscale modeling and quality control in multidimensional case, *Comput. Methods Appl. Mech. Engrg.* 126 (1) (1995) 17–38.
- [13] S.J. Hollister, N. Kikuchi, A comparison of homogenization and standard mechanics analyses for periodic porous composites, *Comput. Mech.* 10 (2) (1992) 73–95.
- [14] J. Fish, A. Wagiman, Multiscale finite element method for a locally nonperiodic heterogeneous medium, *Computational mechanics* 12 (3) (1993) 164–180.
- [15] J. Fish, K. Shek, M. Pandheeradi, M.S. Shephard, Computational plasticity for composite structures based on mathematical homogenization: Theory and practice, *Comput. Methods Appl. Mech. Engrg.* 148 (1) (1997) 53–73.
- [16] P. Suquet, Local and global aspects in the mathematical theory of plasticity, in: *Plasticity Today: Modelling, Methods and Applications*, 1985, pp. 279–310.
- [17] F. Feyel, Multiscale fe 2 elastoviscoplastic analysis of composite structures, *Comput. Mater. Sci.* 16 (1) (1999) 344–354.
- [18] F. Feyel, J.-L. Chaboche, Fe 2 multiscale approach for modelling the elastoviscoplastic behaviour of long fibre sic/ti composite materials, *Comput. Methods Appl. Mech. Engrg.* 183 (3) (2000) 309–330.
- [19] C.V. Verhoosel, J.J. Remmers, M.A. Gutiérrez, R. De Borst, Computational homogenization for adhesive and cohesive failure in quasi-brittle solids, *Internat. J. Numer. Methods Engrg.* 83 (8–9) (2010) 1155–1179.
- [20] C.V. Verhoosel, J.J. Remmers, M.A. Gutiérrez, A partition of unity-based multiscale approach for modelling fracture in piezoelectric ceramics, *Internat. J. Numer. Methods Engrg.* 82 (8) (2010) 1–28.
- [21] V.P. Nguyen, O. Lloberas-Valls, M. Stroeven, L.J. Sluys, Homogenization-based multiscale crack modelling: from micro-diffusive damage to macro-cracks, *Comput. Methods Appl. Mech. Engrg.* 200 (9) (2011) 1220–1236.
- [22] V.P. Nguyen, O. Lloberas-Valls, M. Stroeven, L.J. Sluys, Computational homogenization for multiscale crack modeling. implementational and computational aspects, *Internat. J. Numer. Methods Engrg.* 89 (2) (2012) 192–226.
- [23] C. Oskay, J. Fish, Eigendeformation-based reduced order homogenization for failure analysis of heterogeneous materials, *Comput. Methods Appl. Mech. Engrg.* 196 (7) (2007) 1216–1243.
- [24] C. Oskay, J. Fish, On calibration and validation of eigendeformation-based multiscale models for failure analysis of heterogeneous systems, *Computational mechanics* 42 (2) (2008) 181–195.
- [25] Z. Yuan, J. Fish, Multiple scale eigendeformation-based reduced order homogenization, *Comput. Methods Appl. Mech. Engrg.* 198 (21) (2009) 2016–2038.
- [26] P. Spanos, A. Kontos, A multiscale monte carlo finite element method for determining mechanical properties of polymer nanocomposites, *Probab. Eng. Mech.* 23 (4) (2008) 456–470.
- [27] J. Fish, W. Wu, A nonintrusive stochastic multiscale solver, *Internat. J. Numer. Methods Engrg.* 88 (9) (2011) 862–879.
- [28] M.J. Bogdanor, S. Mahadevan, C. Oskay, Uncertainty quantification in damage modeling of heterogeneous materials, *Int. J. Multiscale Comput. Eng.* 11 (3) (2013) 1–33.
- [29] M.J. Bogdanor, C. Oskay, S.B. Clay, Multiscale modeling of failure in composites under model parameter uncertainty, *Computational mechanics* 56 (3) (2015) 389–404.
- [30] M. Mosby, K. Matouš, Hierarchically parallel coupled finite strain multiscale solver for modeling heterogeneous layers, *Internat. J. Numer. Methods Engrg.* 102 (3–4) (2015) 748–765.
- [31] M. Kästner, G. Haasemann, V. Ulbricht, Multiscale XFEM-modelling and simulation of the inelastic material behaviour of textile-reinforced polymers, *Internat. J. Numer. Methods Engrg.* 86 (4–5) (2011) 477–498.
- [32] G. Legrain, P. Cartraud, I. Perreard, N. Moës, An X-FEM and level set computational approach for image-based modelling: Application to homogenization, *Internat. J. Numer. Methods Engrg.* 86 (7) (2011) 915–934.
- [33] B. Hiriyur, H. Waisman, G. Deodatis, Uncertainty quantification in homogenization of heterogeneous microstructures modeled by XFEM, *Internat. J. Numer. Methods Engrg.* 88 (3) (2011) 257–278.
- [34] D. Savvas, G. Stefanou, M. Papadrakakis, G. Deodatis, Homogenization of random heterogeneous media with inclusions of arbitrary shape modeled by XFEM, *Computational mechanics* 54 (5) (2014) 1221–1235.
- [35] M.G. Pike, C. Oskay, XFEM modeling of short microfiber reinforced composites with cohesive interfaces, *Finite Elem. Anal. Des.* 106 (2015) 16–31.
- [36] M.G. Pike, M.A. Hickman, C. Oskay, Interactions between multiple enrichments in extended finite element analysis of short fiber reinforced composites, *International journal for multiscale computational engineering* 13 (6) (2015) 1–37.
- [37] F. Radtke, A. Simone, L. Sluys, A partition of unity finite element method for simulating non-linear debonding and matrix failure in thin fibre composites, *Internat. J. Numer. Methods Engrg.* 86 (4–5) (2011) 453–476.

- [38] A. Clément, C. Soize, J. Yvonnet, Computational nonlinear stochastic homogenization using a nonconcurrent multiscale approach for hyperelastic heterogeneous microstructures analysis, *Internat. J. Numer. Methods Engrg.* 91 (8) (2012) 799–824.
- [39] A. Clément, C. Soize, J. Yvonnet, Uncertainty quantification in computational stochastic multiscale analysis of nonlinear elastic materials, *Comput. Methods Appl. Mech. Engrg.* 254 (2013) 61–82.
- [40] C. Miehe, M. Hofacker, F. Welschinger, A phase field model for rate-independent crack propagation: Robust algorithmic implementation based on operator splits, *Comput. Methods Appl. Mech. Engrg.* 199 (45) (2010) 2765–2778.
- [41] M.J. Borden, C.V. Verhoosel, M.A. Scott, T.J. Hughes, C.M. Landis, A phase-field description of dynamic brittle fracture, *Comput. Methods Appl. Mech. Engrg.* 217 (2012) 77–95.
- [42] C. McAuliffe, H. Waisman, On the importance of nonlinear elastic effects in shear band modeling, *Int. J. Plast.* 71 (2015) 10–31.
- [43] C. McAuliffe, H. Waisman, A unified model for metal failure capturing shear banding and fracture, *Int. J. Plast.* 65 (2015) 131–151.
- [44] C. Miehe, L.-M. Schänel, Phase field modeling of fracture in rubbery polymers. Part i: Finite elasticity coupled with brittle failure, *J. Mech. Phys. Solids* 65 (2014) 93–113.
- [45] B. Bourdin, G.A. Francfort, J.-J. Marigo, Numerical experiments in revisited brittle fracture, *J. Mech. Phys. Solids* 48 (4) (2000) 797–826.
- [46] G.A. Francfort, J.-J. Marigo, Revisiting brittle fracture as an energy minimization problem, *Journal of the mechanics and physics of solids* 46 (8) (1998) 1319–1342.
- [47] H. Stumpf, K. Hackl, Micromechanical concept for the analysis of damage evolution in thermo-viscoelastic and quasi-brittle materials, *Int. J. Solids Struct.* 40 (6) (2003) 1567–1584.
- [48] B. Bourdin, G.A. Francfort, J.-J. Marigo, The variational approach to fracture, *J. Elasticity* 91 (1–3) (2008) 5–148.
- [49] E.M. Arruda, M.C. Boyce, A three-dimensional constitutive model for the large stretch behavior of rubber elastic materials, *Journal of the mechanics and physics of solids* 41 (2) (1993) 389–412.
- [50] T. Belytschko, W.K. Liu, B. Moran, K. Elkhodary, *Nonlinear Finite Elements for Continua and Structures*, John Wiley & Sons, 2013.
- [51] R.W. Ogden, *Non-Linear Elastic Deformations*, Courier Corporation, 1997.
- [52] S. Hiermaier, *Structures Under Crash and Impact: Continuum Mechanics, Discretization and Experimental Characterization*, Springer Science & Business Media, 2007.
- [53] A.F. Bower, *Applied Mechanics of Solids*, CRC press, 2009.
- [54] N.A. Hocine, M.N. Abdelaziz, A. Imad, Fracture problems of rubbers: J-integral estimation based upon η factors and an investigation on the strain energy density distribution as a local criterion, *Int. J. Fract.* 117 (1) (2002) 1–23.
- [55] T. Koga, T. Hashimoto, M. Takenaka, K. Aizawa, N. Amino, M. Nakamura, D. Yamaguchi, S. Koizumi, New insight into hierarchical structures of carbon black dispersed in polymer matrices: A combined small-angle scattering study, *Macromolecules* 41 (2) (2008) 453–464.
- [56] R.L. Taylor, Feap-a Finite Element Analysis Program, Programmer Manual, University of California, Berkeley, <http://www.ce.berkeley.edu/feap>.
- [57] C. Geuzaine, J.-F. Remacle, *Gmsh Reference Manual*, Free Software Foundation Inc., USA.
- [58] A. Henderson, Paraview Guide, A Parallel Visualization Application, kitware inc., 2005, URL <http://www.paraview.org>.
- [59] J.D. Hunter, Matplotlib: A 2d graphics environment, *Comput. Sci. Eng.* 9 (3) (2007) 90–95.
- [60] S. Balay, S. Abhyankar, M. Adams, J. Brown, P. Brune, K. Buschelman, V. Eijkhout, W. Gropp, D. Kaushik, M. Knepley, et al., *Petsc Users Manual Revision 3.5*, Tech. Report, Argonne National Laboratory (ANL), 2014.
- [61] T.A. Davis, I.S. Duff, An unsymmetric-pattern multifrontal method for sparse lu factorization, *SIAM J. Matrix Anal. Appl.* 18 (1) (1997) 140–158.
- [62] J. Bonet, R.D. Wood, *Nonlinear Continuum Mechanics for Finite Element Analysis*, Cambridge university press, 1997.